ANNUAL REVIEWS

Annual Review of Earth and Planetary Sciences

A 2020 Observational Perspective of Io

Imke de Pater,[1] James T. Keane,[2] Katherine de Kleer,[3] and Ashley Gerard Davies[2]

[1]Department of Astronomy, University of California, Berkeley, California 94720, USA; email: imke@berkeley.edu

[2]Jet Propulsion Laboratory, California Institute of Technology, Pasadena, California 91109, USA

[3]Division of Geological and Planetary Sciences, California Institute of Technology, Pasadena, California 91125, USA

Annu. Rev. Earth Planet. Sci. 2021. 49:643–78

First published as a Review in Advance on March 23, 2021

The *Annual Review of Earth and Planetary Sciences* is online at earth.annualreviews.org

https://doi.org/10.1146/annurev-earth-082420-095244

Keywords

Galilean satellites, Io, astronomical observations, atmosphere, volcanism

Abstract

Jupiter's Galilean satellite Io is one of the most remarkable objects in our Solar System. The tidal heating Io undergoes through its orbital resonance with Europa and Ganymede has resulted in a body rich in active silicate volcanism. Over the past decades, Io has been observed from ground-based and Earth-orbiting telescopes and by several spacecraft. In this review we summarize the progress made toward our understanding of the physical and chemical processes related to Io and its environment since the *Galileo* era. Io science has been revolutionized by the use of adaptive optics techniques on large, 8- to 10-m telescopes. The resultant ever-increasing database, mapping the size, style, and spatial distribution of Io's diverse volcanoes, has improved our understanding of Io's interior structure, its likely composition, and the tidal heating process. Additionally, new observations of Io's atmosphere obtained with these large optical/infrared telescopes and the Atacama Large Millimeter/submillimeter Array reveal the presence of volcanic plumes, the (at times) near-collapse of Io's atmosphere during eclipse, and the interactions of plumes with the sublimation atmosphere.

- Extensive new data sets of Io at ultraviolet, mid- to near-infrared, and radio wavelengths have been gathered since the *Galileo* era.
- New data and models inform us about tidal heating, surface properties, and magma composition across Io—although key questions remain.

- Atmospheric observations indicate a dominant sublimation-supported component and reinforce the presence of stealth volcanism.
- Observations of volcanic plumes show high gas velocities (up to ~1 km/s) and their effect on Io's atmosphere.

1. INTRODUCTION

Jupiter's satellite Io is our Solar System's most volcanically active body, with a heat flow (W m^{-2}) ~30 times that of present-day Earth (Matson et al. 1981). Roughly 55% of Io's heat flow has been attributed to volcanic hot spots (Veeder et al. 2015). Near-infrared images—in particular those taken with Io in Jupiter's shadow (eclipse) at high spatial resolution, such as obtained by spacecraft or by using adaptive optics (AO) techniques on large (8–10 m) ground-based telescopes—reveal dozens of thermally bright volcanic hot spots (**Figure 1**). Some hot spots are associated with active plumes, which are a major source of material into Io's atmosphere and Jupiter's magnetosphere and even pollute the interplanetary medium. This widespread volcanic activity is powered by strong tidal heating induced by Io's orbital eccentricity, which is the result of the Laplace (4:2:1) orbital resonance among Io, Europa, and Ganymede (Peale et al. 1979). Io is the Solar System's primary example of extreme tidal heating and the only known body beyond Earth where we can consistently observe high-temperature volcanic activity *now*.

Io has been observed since Galileo Galilei's discovery of Jupiter's four large moons in 1610, and more modern ground- and space-based telescopes have provided a vast database of multiwavelength observations over the past ~50 years. However, we still do not understand the inner workings of this satellite, such as where the tidal heat is dissipated, how the heat is released, how volcanic eruptions and their characteristics (e.g., gas content, eruption energetics, lava composition) relate to the deeper interior, and what their effect is on the atmosphere. By studying these processes on Io, we hope to learn more about tidal heating, a fundamental process that has applications for exoplanets and for understanding of the habitability of tidally heated icy moons such as Europa and Enceladus. In addition, a deeper understanding of voluminous effusive volcanism will shed light on the formative years of the terrestrial worlds in our Solar System, including Earth and its Moon.

This review focuses on results from Earth-based observations obtained since the *Galileo* era. Extensive reviews of the state of knowledge through the *Galileo* era are published in the books *Volcanism on Io: A Comparison with Earth* (Davies 2007), *Io After* Galileo (Lopes & Spencer 2007), and *Jupiter: The Planet, Satellites and Magnetosphere* (Bagenal et al. 2004). Since *Galileo*, a wealth of new observations have been obtained from Earth (surface and orbit) via remote sensing at ultraviolet (UV), visible, near- and mid-infrared, and (sub)millimeter wavelengths. For completeness, we also provide a brief review of spacecraft results and geophysical research that have been published since the last major Io reviews. In the following sections we separately discuss observations pertaining to Io's interior, surface, and atmosphere.

2. IO'S INTERIOR

Since the *Galileo* era, there have been major advances in our understanding of Io's interior structure and evolution and the fundamental process of tidal heating. These geophysical advances provide the context for interpreting Earth-based observations, which are often designed to interrogate Io's interior structure and evolution from afar. In this section, we summarize the most notable developments in our understanding of Io's geophysics since the close of the *Galileo* mission.

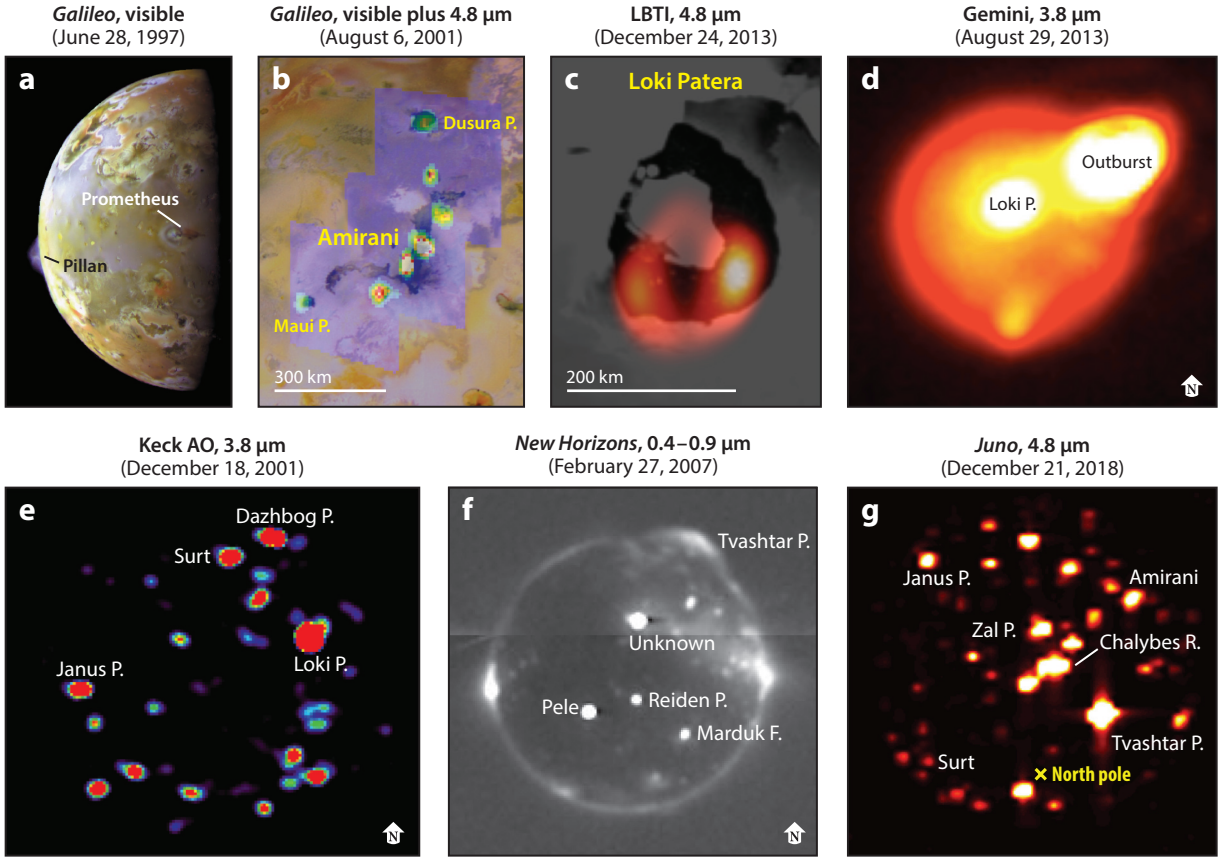

Figure 1

Example observations of Io at visible and near-infrared wavelengths in sunlight (*panels a–d*) and in eclipse (*panels e–g*). The spacecraft or telescope, wavelength, and date are indicated at the top of each panel, and several volcanic features are indicated (P stands for Patera, F for Fluctus, and R for Regio). Although spacecraft observations exhibit superb spatial resolution, we note that the 40–50-milliarcsecond (140–160 km on Io's disk) resolution of ground-based infrared adaptive optics (AO) images from 8- to 10-m telescopes is quite similar to most near-infrared images taken by spacecraft. (*a*) *Galileo* visible-light image. The 140-km-high plume from Pillan is seen on the limb, and the (reddish) shadow of a plume from Prometheus is at the center of Io. Image provided by NASA/JPL/UofA. (*b*) Amirani lava flows at visible wavelengths with superposed 4.8-μm hot spots, indicative of active volcanism. Image provided by NASA/JPL/UofA. (*c*) Large Binocular Telescope Interferometer (LBTI) image of Loki Patera (*orange*; 4.8 μm) superposed on a *Voyager* image of the volcanic depression. The original LBTI image was smoothed to better indicate the location of the two distinct emission features. Image provided by LBTO/NASA; adapted from Conrad et al. (2015). (*d*) AO observations of Io when a bright outburst east of Loki Patera was detected. Image modified with permission from de Kleer et al. (2014). (*e*) AO observations of Io in eclipse. Image modified with permission from de Pater et al. (2004). (*f*) *New Horizons* image of Io in eclipse. A 330-km-high plume is visible above Tvashtar Paterae. The edge of Io's disk is outlined by a faint auroral glow, with much brighter glows on the left and right sides of Io's disk. These glows are manifestations of interactions between the atmosphere and magnetospheric plasma. Image provided by NASA/JHU/APL/SwRI. (*g*) *Juno* observations of Io in eclipse, looking down on the north pole. Image provided by NASA/JPL-Caltech/SwRI/ASI/INAF/JIRAM.

2.1. Constraints on Io's Interior Structure

2.1.1. Long-wavelength shape. The long-wavelength or global shape of Io is set by a combination of rotational and tidal forces (for a review, see Murray & Dermott 1999). The combination of these two forces predicts an equilibrium shape described as a triaxial ellipsoid. The long axis

Table 1 Io's bulk properties

Parameter	Value	Description	Reference
a	1,831.1 ± 0.3 km	Triaxial figure, longest semimajor axis (tidal axis)	Oberst & Schuster 2004
b	1,820.4 ± 0.5 km	Triaxial figure, intermediate semimajor axis	Oberst & Schuster 2004
c	1,816.6 ± 0.5 km	Triaxial figure, shortest semimajor axis (spin axis)	Oberst & Schuster 2004
R_{mean}	1,822.7 ± 0.2 km	Mean radius, $R_{mean} = (abc)^{1/3}$	—
GM	5,959.91 ± 0.02 km^2 s^{-2}	Gravitational constant[a]	Jacobson 2013
ρ	3,527.5 ± 2.9 kg m^{-3}	Density	Schubert et al. 2004
J_2	(1,846.7 ± 3.6) × 10^{-6}	Gravity field[a]	Jacobson 2013
C_{21}	(4.4 ± 0.9) × 10^{-6}	Gravity field[a]	Jacobson 2013
S_{21}	(−2.9 ± 2.0) × 10^{-6}	Gravity field[a]	Jacobson 2013
C_{22}	(556.4 ± 0.6) × 10^{-6}	Gravity field[a]	Jacobson 2013
S_{22}	(0.6 ± 0.6) × 10^{-6}	Gravity field[a]	Jacobson 2013
k_2^f	1.3043 ± 0.0019	Degree-2 fluid potential Love number	Schubert et al. 2004
b_2^f	2.242 ± 0.167	Degree-2 fluid displacement Love number	Moore et al. 2007

[a]Reference radius for gravity model is 1,821.6 km (Jacobson 2013). Spherical harmonic normalization follows Schubert et al. (2004).

(a) is aligned with Jupiter (the tidal axis that defines 0°W and 180°W in Io's longitude system). The intermediate axis (b) is aligned with Io's orbital velocity vector (90°W and 270°W). The short axis (c) is aligned with Io's spin pole (defining 90°N and 90°S). At present, Io's triaxial shape is moderately well constrained from *Voyager* and *Galileo* images (**Table 1**).

2.1.2. Short-wavelength shape. At local scales, Io's shape is affected by an array of geological and geophysical processes (**Figure 2*b***). White et al. (2014) present the most complete topography model for Io derived from a stereophotogrammetry analysis of overlapping *Voyager* and *Galileo* images. This topography model covers approximately 75% of Io, albeit with varying vertical and horizontal resolutions (hundreds of meters to several kilometers).

One of the most widely debated features in Io's short-wavelength topography is the identification of putative basins and swells. In early control-point analyses, Gaskell et al. (1988) identified broad (~500-km diameter), low-amplitude (±1 km), alternating patterns of basins and swells separated by 90° of arc. If these features exist, they may reflect tidal heating patterns at depth and/or the processes by which that heat escapes Io (e.g., Ross et al. 1990). While basins and swells have motivated substantial theoretical research, subsequent topography analyses have not consistently identified basins and swells or identified basins and swells in different regions. The White et al. (2014) model does identify several longitudinally arranged basins and swells that appear correlated with the spatial distribution of mountains and volcanoes, respectively.

2.1.3. Gravity. Gravity measurements, acquired by precise Doppler tracking of spacecraft flybys, provide direct constraints on the distribution of mass within a planetary body. Gravity models are usually written in terms of spherical harmonic coefficients, C_{lm} and S_{lm}, where l and m are the degree and order of the solution. Larger degree/order corresponds to shorter wavelength (for a review of planetary gravity methods, see Wieczorek 2015).

The current state of knowledge of Io's gravity field is severely limited due to the small number of close flybys, flyby geometry, and overall data quality from *Voyager* and *Galileo*. The immediate post-*Galileo* gravity analysis (Anderson et al. 2001, Schubert et al. 2004) retrieved only a partial degree-2 gravity field: J_2 (the gravity equivalent of oblateness) and C_{22} (which quantifies how Io is

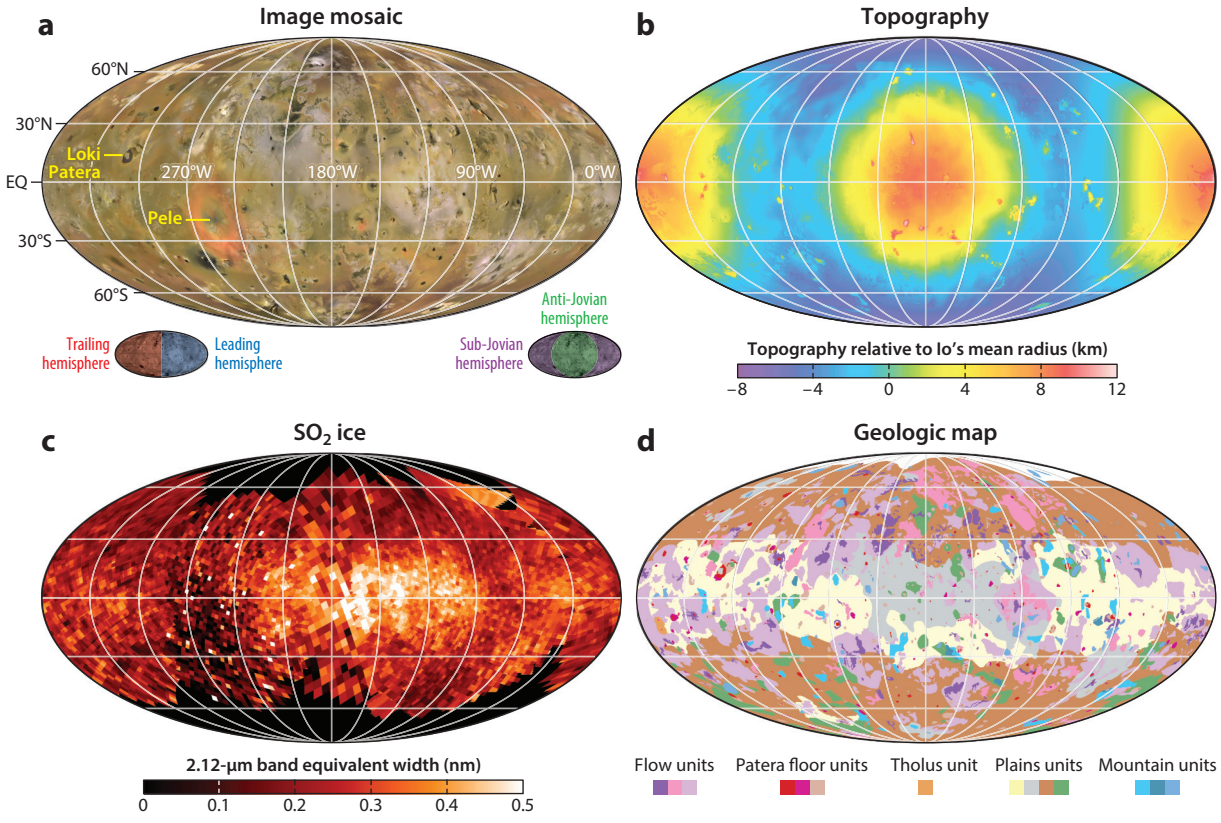

Figure 2

A global view of Io's surface, topography, and geology. (*a*) Merged *Galileo* and *Voyager* image mosaic. Image provided by NASA/JPL/USGS. (*b*) Topography of Io, combining the long-wavelength triaxial figure (Oberst & Schuster 2004) with the short-wavelength, stereo-derived topography (White et al. 2014). Gaps in the stereotopography can be identified by the lack of small-scale structure. Topography is referenced to the mean radius of Io (1,822.7 km). (*c*) SO_2 ice map, shown in the form of the 2.12-μm equivalent width (de Pater et al. 2020a). (*d*) Abbreviated geologic map of Io (Williams et al. 2011). All maps are in Mollweide projection, centered on 180°W (the anti-Jovian hemisphere).

stretched toward Jupiter). However, these coefficients were not independent because the models assumed Io to be in hydrostatic equilibrium (where $J_2/C_{22} = 10/3$). More recently, Jacobson (2013) reanalyzed the *Galileo* data, producing a complete degree-2 gravity field for Io (**Table 1**) that hints at some nonhydrostatic effects (indicated by the slight nonzero C_{21}) but still provides only moderate improvements to our understanding of Io's interior structure (Section 2.2). The current state of knowledge of Io's gravity field is comparable to our knowledge of Earth's Moon's before the *Apollo* era.

Thus far, all gravity measurements have been of Io's static gravity field—i.e., the unchanging, time-averaged gravity field. However, time-varying gravity would be a powerful tool for probing Io's interior structure. Io's degree-2 potential Love number, k_2, quantifies how a body's gravitational potential responds to an external, time-varying forcing potential. We distinguish between the fluid Love number, k_2^f, and the tidal Love number, k_2^t. k_2^f describes Io's response to the long-term, time-averaged forcing potential and is captured in the static degree-2 gravity field (**Table 1**). It is related to the interior density distribution and (under certain assumptions) to the

body's moment of inertia (the Radau-Darwin approximation) (Darwin 1899, Murray & Dermott 1999). In contrast, k_2^t describes how Io responds on a tidal timescale (i.e., Io's orbital period: 42 h) and would yield information about Io's viscoelastic response to tides, the thickness and rigidity of the lithosphere, and the presence of a magma ocean. For example, if Io is completely solid, k_2^t is ∼0.09, while k_2^t is ∼0.5 if it has a fluid magma ocean (Bierson & Nimmo 2016, de Kleer et al. 2019d).

Because planetary materials do not respond perfectly elastically, we expect a phase lag between the tidal forcing potential and Io's response. This phase lag is directly related to Io's rigidity and viscosity and the energy dissipation rate within Io expressed as k_2^t/Q, where Q is the tidal dissipation quality factor. Unfortunately, this phase lag has not been directly measured, although it has been estimated using different methods, including assuming that Io's tidal dissipation is in equilibrium with Io's orbital evolution (Section 2.4) or that Io's tidal dissipation can be inferred from Io's thermal output (Section 3.3).

While we have focused on the gravitational potential Love number, k_2, it is worth noting that it is also possible to measure how Io's shape responds to tides with the radial and lateral surface displacement Love numbers, h_2 and l_2, respectively. These surface displacement Love numbers can be divided in the same way as described above, and like for k_2, only Io's h_2^f is measured (Moore et al. 2007) (**Table 1**). k_2, h_2, and l_2 have similar—but not identical—dependencies on Io's interior structure, rheology, and energy dissipation. Like k_2^t, for a solid Io, h_2^t is ∼0.1, and h_2^t is ∼0.5–1.0 for an Io with a fluid magma ocean (de Kleer et al. 2019d).

2.1.4. Magnetic induction. As Io orbits Jupiter, it is subjected to a time-varying external magnetic field (because Jupiter's magnetic field is inclined with respect to Io's orbital plane). In the reference frame of Io, the applied magnetic field oscillates at Jupiter's synodic period (12.95 h), generating eddy currents within Io's conductive layers, producing an induced magnetic field. The strength and geometry of this induced field vary as the applied external field varies and are sensitive to the electrical properties within Io. (This is distinct from a core dynamo, which would be largely insensitive to these external perturbations.) Through the use of laboratory measurements of analogs, it is possible to interpret these magnetic field anomalies in terms of melt fraction, depth distribution, composition, and temperature (e.g., Khan et al. 2014, Pommier et al. 2015). Magnetic induction (or magnetic sounding) has been well demonstrated at Earth and the Moon (Hood et al. 1982, Constable & Constable 2004) and used to detect salty (i.e., conductive) subsurface water oceans on Europa (Khurana et al. 1998, Kivelson et al. 2000), Ganymede (Zimmer et al. 2000, Kivelson et al. 2002), and Callisto (Khurana et al. 1998, Zimmer et al. 2000). While magnetic induction is traditionally deduced from in situ magnetic field and plasma measurements, there have been recent attempts to use Earth-based observations of aurora to sound the interiors of the Galilean satellites [e.g., Ganymede (Saur et al. 2015)]. Aurora respond to both the external and induced fields and provide complementary insights, although the technique lacks the precision of in situ measurements.

Analysis of *Galileo* magnetometer data revealed the presence of an induced magnetic field at Io (Khurana et al. 2011). The induced field is global, dipolar, time varying, and out of phase with the applied field—confirming that it is not a permanent dynamo. By modeling the induced magnetic field, Khurana et al. (2011) showed that the induced signal was inconsistent with a completely solid mantle and was best fit by a $\gtrsim$50-km-thick shell of $\gtrsim$20% partial melt located ∼50 km beneath the surface—consistent with the presence of a subsurface magma ocean (Section 2.2). At present, this is the best evidence for an extant magma ocean within Io, although this has been the subject of extensive debate within the community. Roth et al. (2017) found that *Hubble Space Telescope* (*HST*) observations of Io's auroral spots [in conjunction with magnetohydrodynamic (MHD)

simulations] were inconsistent with the presence of a Khurana et al. (2011)–style magma ocean and instead favored either atmosphere-plasma interactions or induction in Io's metallic core. The same group later modeled the *Galileo* magnetometer data with a more complex three-dimensional (3D) MHD model and found that plasma interactions with Io's asymmetric atmosphere could equally explain the observed magnetic field signal (Blöcker et al. 2018). A third group, Šebek et al. (2019), subsequently performed independent MHD models and strongly favored the presence of an induced magnetic field from a magma ocean. In short, the nature of Io's induced magnetic field and the presence of a subsurface magma ocean are still uncertain.

2.2. Models for Io's Interior Structure (and the Magma Ocean Hypothesis)

From the geophysical constraints outlined above, it is possible to construct a simplified model of Io's interior structure. Io's bulk density (**Table 1**) coupled with the presence of silicate volcanism at the surface strongly implies a rocky (i.e., silicate) interior. Io's fluid Love numbers k_2^f and h_2^f (Sections 2.1.1–2.1.3) are smaller than those for a homogeneous body [$k_2^f = 3/2$ and $h_2^f = 5/2$ (e.g., Murray & Dermott 1999)], suggesting that density increases with depth, consistent with a differentiated Io. Beyond this, the available geophysical data constrain only families of interior structure models (Anderson et al. 2001, Schubert et al. 2004, Moore et al. 2007). Typical model solutions consist of an Fe-rich core with a radius of 0.35 (pure Fe composition) to 0.50 (Fe-FeS eutectic composition) Io radii, overlain by a silicate-rich (olivine or orthopyroxene) mantle and lower density crust built from recycling erupted basaltic and sulfurous lava flows (Moore et al. 2007). The lithosphere is likely tens to hundreds of kilometers thick in order to support Io's tall mountains (Turtle et al. 2007).

The single largest outstanding question about Io's interior structure is whether it possesses an extant magma ocean, defined as a global, continuous fluid melt layer analogous to the subsurface water oceans within many icy ocean worlds (e.g., Nimmo & Pappalardo 2016). While the presence of a magma ocean within Io has been argued on theoretical grounds (e.g., Peale et al. 1979, Keszthelyi et al. 1999), the best evidence comes from magnetic induction studies (Section 2.1.4). While this analysis is debated, if we follow Khurana et al. (2011), Io has a subsurface layer with a melt fraction $\gtrsim$20%. While this is often used to argue for the presence of a subsurface magma ocean (as in Khurana et al. 2011), we note that a melt fraction of $\sim$20% does not necessarily imply disaggregation (where grains become supported by fluid). Thus, it is still unclear whether the magnetic induction signature betrays a true magma ocean or a region of partial melt.

2.3. Theoretical Models for Tidal Heating and Heat Transport Within Io

Classic tidal heating models assume that Io is predominantly solid, with dissipation occurring entirely within the solid layers (e.g., Segatz et al. 1988, Ross et al. 1990, Tackley et al. 2001, Tobie et al. 2005, Hamilton et al. 2013, Steinke et al. 2020). However, recent research has shown that tidal dissipation in the fluid layers—like Io's magma ocean—may be important. Dissipation in a subsurface magma (or water) ocean may produce different heating patterns than solid-body dissipation alone, including breaking the usual symmetry about the tidal/orbital symmetry axes. This may explain Io's eastward shift in volcanic features (Section 3) and heat flow (Section 3.3) (e.g., Soderlund et al. 2014, Matsuyama et al. 2018, Hay & Matsuyama 2019). **Figure 3** shows three example end-member models for tidal heating within Io. While tidal heating models have advanced, there are still notable deficiencies in available models. First, more realistic model rheologies are required to accurately capture the physics occurring within Io and other tidally heated worlds (e.g.,

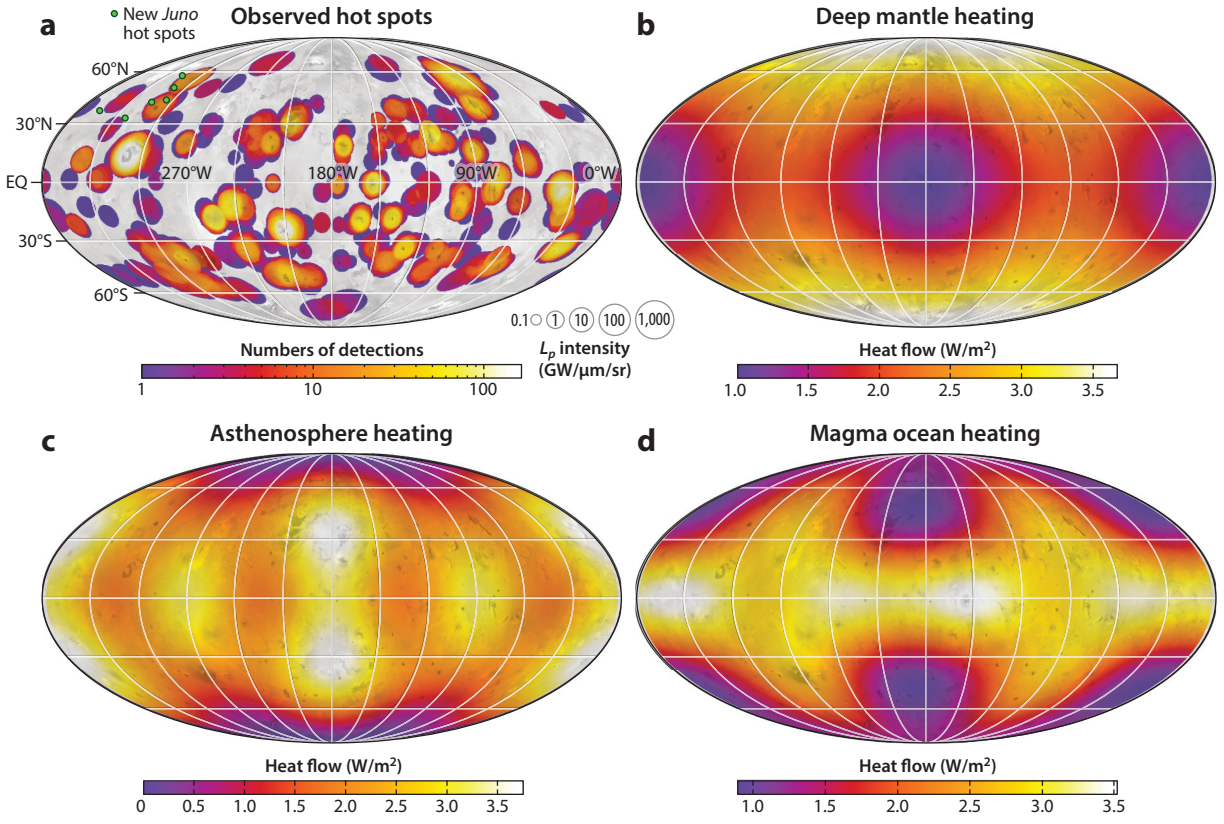

Figure 3

Io's hot spots and theoretical models for Io's heat flow. (*a*) Io's hot spots, as observed from ground-based telescopes [L_p-band, 3.4–4.1 μm (Marchis et al. 2002, de Kleer & de Pater 2016b, Cantrall et al. 2018, de Kleer et al. 2019b)] and *Galileo* Near Infrared Mapping Spectrometer (NIMS) [4.5–5 μm (Davies et al. 2012; Veeder et al. 2012, 2015)]. The size of each point corresponds to the brightness, and the color indicates the number of times that hot spot was observed. NIMS 4.8–5-μm intensities were divided by 2 to more closely match ground-based L_p-band (3.8 μm) observations. New hot spots identified by *Juno* JIRAM are shown as green points [as they have not been quantified like the other data points (Mura et al. 2020)]. (*b–d*) Three end-member models for tidal dissipation within Io, including solid-body dissipation heating in Io's deep mantle (*b*) or asthenosphere (*c*), or fluid-body dissipation in a magma ocean (*d*). Models courtesy of Isamu Matsuyama (de Kleer et al. 2019d).

Renaud & Henning 2018). Developing these model rheologies requires laboratory experiments at relevant pressures, temperatures, and frequencies. Second, most tidal heating models assume that heat dissipated (or melt generated) in a parcel at depth is instantaneously transported vertically to the surface. New models by Steinke et al. (2020) are a notable exception, as they include the blurring effect of mantle convection and a simplified melt migration model. Nonetheless, melt migration through Io's mantle and crust is complicated, perhaps resulting in subcrustal layers of melt or magmatic intrusions (Spencer et al. 2020). Third, most models assume (or require) axisymmetry and cannot capture effects from lateral variations in bulk properties (e.g., crustal thickness variations). Finally, few models consider the probable feedbacks between tidal heating and interior structure, such as changes in viscosity, and therefore the efficacy of tidal dissipation. Models that have investigated this show that such feedbacks may scramble classical results (Steinke et al. 2019).

2.4. Orbital Evolution of Io

The mechanics of Io's tidal heating can also be studied through measurements of its orbital evolution. Through the tidal bulge that Io raises on Jupiter, Jupiter's rotational energy is ultimately converted into heat in Io's interior and alters Io's orbit. Constraints on these orbital changes can therefore inform our understanding of heat dissipation in both Io and Jupiter.

High-precision measurements of the relative position of Io are needed to detect the orbital changes, which are on the order of tens of kilometers over decade timescales. The most precise measurements from Earth are obtained by mutual occultations of the satellites (which occur every 6 years), occultations of stars by the satellites (which are valuable but rare), and radar ranging. Radar ranging from Arecibo has obtained the most precise positional measurements on Io from Earth to date, with a precision of just over 5 km (Brozović et al. 2020). Past research has found contradictory results for the magnitude and direction of Io's secular orbital evolution (e.g., Goldstein & Jacobs 1995, Aksnes & Franklin 2001). The most recent calculations find a secular mean-motion acceleration of $+(0.14 \pm 0.01) \times 10^{-10}$ year^{-1} (Lainey et al. 2009), indicating that Io's orbit is currently moving inward, while Europa and Ganymede are moving outward. Fits to the orbital model used in this study yielded a dissipation ratio k_2'/Q of 0.015 ± 0.003 for Io, which predicts a heat flow of $(9.33 \pm 1.87) \times 10^{13}$ W. This value is within uncertainties of the measured global heat flow, suggesting that Io is currently in thermal equilibrium.

3. IO'S SURFACE

The *Voyager* and *Galileo* spacecraft imaged Io's surface in detail, revealing the satellite's yellow-white-orange-red coloration (**Figure 2*a***). These surface colors are attributed to SO_2 frost, a variety of sulfur allotropes (S_2–S_{20}), and metastable polymorphs of elemental sulfur mixed in other species (Moses & Nash 1991, Carlson et al. 2007). Numerous dark lava flows and dark-floored paterae (i.e., irregular calderas), many the sites of persistent or intermittent volcanic activity, mark the surface and indicate the presence of silicate lava that may include (ultra)mafic minerals such as olivine and pyroxene (Geissler et al. 1999). The lack of impact craters identified on Io's surface places an upper limit on the surface age of 10^6 to 10^7 years, which implies a volcanic resurfacing rate of order 0.1–1 cm/year (e.g., Carr 1986). Io's otherwise muted topography [which varies across Io's plains by only $\sigma = 0.61$ km relative to the triaxial ellipsoid (White et al. 2014); Section 2.1.1] is interrupted by rugged kilometer-high (up to 17 km) mountains that appear to have formed by the uplift of large blocks of crust (Turtle et al. 2007). To sustain such high mountains, the lithosphere must be at least several tens of kilometers thick, which can be reconciled with the high heat flow via a heat-pipe mechanism in the crust (O'Reilly & Davies 1981) (Section 2.3). **Figure 4** provides a summary of the various surface features and processes.

SO_2 frost is ubiquitous on Io's surface (except near the poles—plausibly a consequence of plasma impact) and has been mapped at wavelengths ranging from 1.98 to 4.07 μm (e.g., McEwen et al. 1988, Schmitt et al. 1994, Carlson et al. 1997, Douté et al. 2001, Laver & de Pater 2009, de Pater et al. 2020a, Tosi et al. 2020). Several of these authors have noted that the various absorption bands have different sensitivities to frost grains of different sizes, where the weakest (1.98 and 2.12 μm) SO_2 frost bands are sensitive only to large-grained (>700 μm) deposits, while the strongest (3.77 and 4.07 μm) absorption bands are sensitive to thin (millimeter-thick or less) veneers of micrometer-sized grains, which appear to be abundant at higher latitudes. The formation of coarse-grained SO_2 snowfields near the equator (**Figure 2*c***) and thin veneers of small-grained frosts at higher latitudes likely results from a combination of sublimation (at low latitudes), condensation (at latitudes greater than 27°), and thermal annealing (at low latitudes) (Geissler et al. 2001, Laver & de Pater 2009).

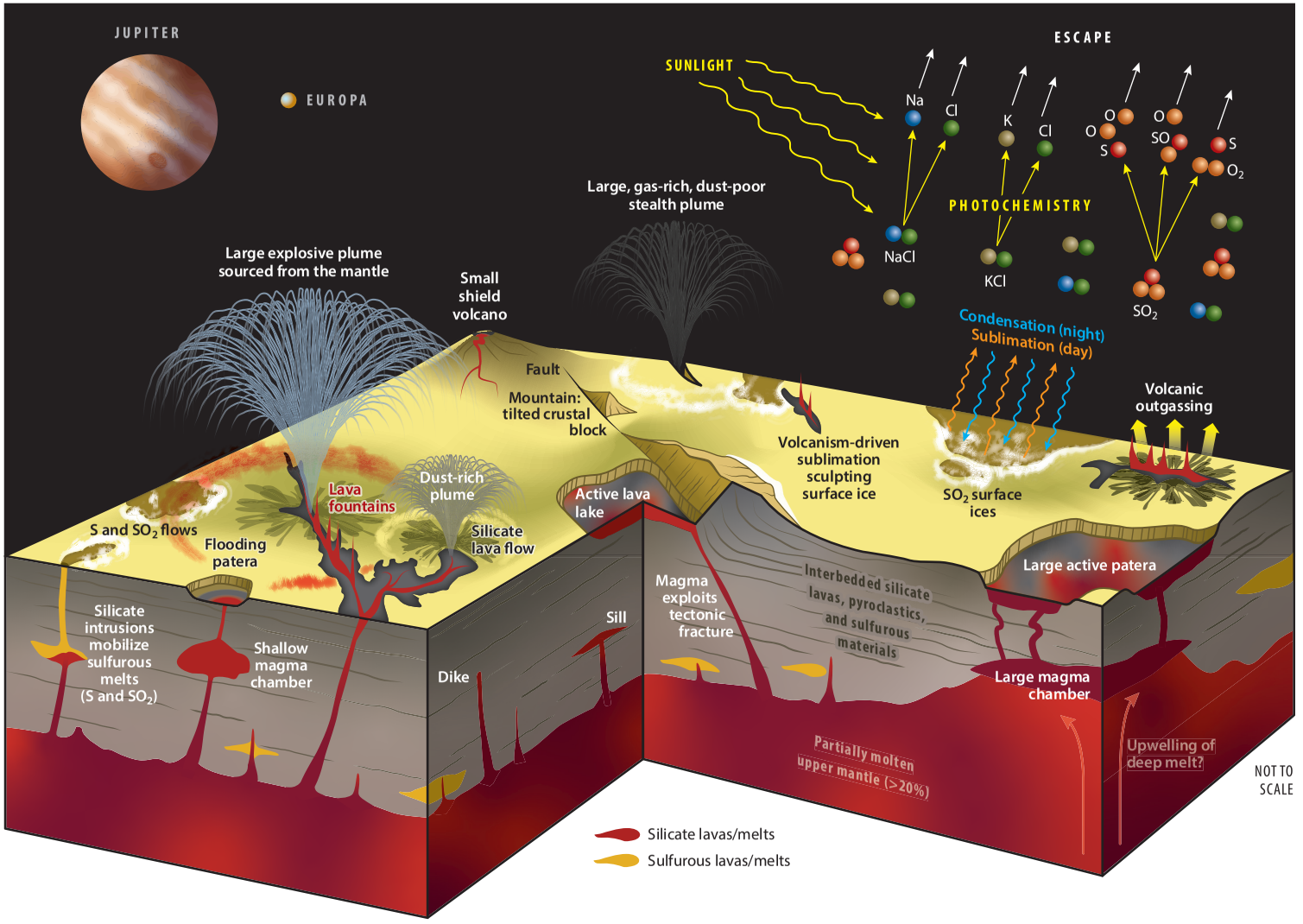

(Caption appears on following page)

Figure 4 (*Figure appears on preceding page*)

A section through Io's crust and atmosphere utilizing what has been learned primarily from *Galileo* and ground-based data analysis. In places, the upper few kilometers of the lithosphere may be rich ($\gtrsim$10%) in sulfur and SO_2. Beneath this layer, compressive and thermal stresses in the lithosphere contribute to mountain building. Faults in the mostly cold lithosphere act as pathways for magma to reach the surface. Silicate magma from deep sources, possibly superheated, erupts in short-lived, sulfur gas–rich explosive events (e.g., Tvashtar Paterae, **Figure 1*f***), although an identical type of plume emanates from the Pele lava lake (**Figure 2*a***). Silicate magma from shallow reservoirs erupts effusively, mobilizing surface volatiles to form dust-rich plumes (e.g., Prometheus, **Figure 1*a***). Silicate magma interacting with SO_2 may result in gas plumes that are hard to detect ("stealth" plumes). Explosive silicate eruptions can generate extensive black plume deposits (e.g., Pillan, in 1997, **Figure 1*a***). Intrusions also mobilize sulfurous material that may erupt at the surface. Patera form by the removal of layers of volatiles above silicate lavas, or by collapse of the magma chamber post-eruption or after magma drainback. Many "active" paterae contain lava lakes or lava flows. The volume of silicate material in intrusions may exceed that extruded by an order of magnitude or more. The lithosphere is at least 30 km thick and is underlain by the partially molten upper mantle of silicate composition with a melt fraction of perhaps 20% or more. SO_2 ice on the surface alternately sublimes (daytime) and condenses (eclipse/night) to keep the vapor pressure near that of the saturated vapor pressure curve. Photochemistry at higher altitudes breaks the molecules apart, leading to the formation of, for example, SO, O, O_2, K, Na, and Cl. The atoms may reside in a neutral cloud or extended corona before being ionized and swept up in the plasma torus. Figure created by Doug Beckner and James Tuttle Keane based on figure 18.1 in Davies (2007).

New analysis of *Voyager* and *Galileo* imagery has enabled the first modern geologic map of Io (Williams et al. 2011) (**Figure 2*d***). This 1:15,000,000 digital map has a resolution that varies from 1 to 20 km. It also includes several derived data products and definitions and mapping of 14 distinct geological units such as paterae, lava flows, mountains, plains, and plume deposits. Of the major categories, plains cover ~67% of the surface, paterae (425 in total) cover ~2.5%, volcanic flows ~28%, and mountains ~3%. This map displays Io's geologic history and provides useful context for other investigations (e.g., White et al. 2014, Cantrall et al. 2018).

3.1. Thermophysical Properties

In contrast to images and spectra of Io taken in reflected sunlight, thermal emission is sensitive to material properties such as emissivity and thermal inertia (which measures how rapidly a material's temperature responds to changes in energy input), which are set by the composition and compactness of the (sub)surface layers. Observations of Io at mid-infrared and radio wavelengths can constrain these quantities as a function of depth in the surface because such observations are sensitive to emission from tens (or even hundreds, for pure, porous ices) of wavelengths deep into a body's crust. By observing Io in sunlight and in eclipse, one can determine these parameters by measuring how fast Io cools at different wavelengths. A sharp drop (~20–30 K, from 127 K) in surface temperature has been observed in the mid-infrared within minutes after entering an eclipse (Morrison & Cruishank 1973, Sinton & Kaminsky 1988, Tsang et al. 2016). At 1 mm, only an ~3-K drop (from 93.6 K) was measured (de Pater et al. 2020b). The combined data suggest that Io's surface is overlain with a thin (no more than a few millimeters thick) low-thermal-inertia layer (50 J m^{-2} K^{-1} $s^{-1/2}$)—such as expected for dust or loose, unconsolidated deposits from volcanic plumes—overlying a more compact high-thermal-inertia layer (320 J m^{-2} K^{-1} $s^{-1/2}$), composed of SO_2 ice and rock (de Pater et al. 2020b). In addition to these vertically stacked layers, the thermal inertia may also vary across the surface, related to frost and nonfrost areas (e.g., Sinton & Kaminsky 1988, Rathbun et al. 2004). Walker et al. (2012) fit a two-component (frost and nonfrost) set of thermal inertias on the surface to *HST* and *Galileo*/photopolarimeter radiometer (PPR) data; such a model needs to be extended to deeper layers using radio observations at high spatial resolution, analogous to the model by de Kleer et al. (2021) for Ganymede.

3.2. Volcanic Eruptions

Io's numerous active volcanic centers appear in visible-infrared ground-based and spacecraft observations as localized areas of enhanced thermal emission (**Figure 1**). These volcanoes exhibit a broad range of different eruption styles, temporal behaviors, and power outputs (Davies et al. 2001). From mostly spacecraft data, more than 250 volcanic centers have been identified to date (Veeder et al. 2012, 2015).

3.2.1. Magma temperature and composition. As an indicator of Io's interior state and the presence (or absence) of a magma ocean, an important outstanding question is whether the silicates erupted on Io are predominantly basalt-like (the most common lava composition on Earth, its Moon, and other terrestrial planets) or hotter ($\gtrsim$1,800 K), magnesium-rich ultramafic lavas (Davies 2007). In the latter case, Io may provide a view of the volcanic processes of Earth's distant past; ultramafic volcanism was once widespread during the Archean (4.0–2.5 Ga) and Proterozoic (2.5–0.5 Ga) eons but is no longer present on Earth. When Io observations catch eruptions during a phase of active lava exposure, the temperatures derived from thermal emission measurements help constrain the composition of the erupting material. *Voyager* long-wavelength infrared data yielded, for the most part, low lava temperatures that were first taken as an indication of sulfur-dominated volcanism (Sagan 1979). Subsequent ground-based observations in 1986 and 1990 at shorter wavelengths (Johnson et al. 1988, Veeder et al. 1994) of powerful outburst eruptions yielded temperatures of ~1,200–1,500 K that could be explained only by voluminous eruptions of silicate lava (e.g., Carr 1986). Further modeling suggested that these eruptions were dominated by silicate lava fountaining (Davies 1996), the only mechanism able to produce such large areas at such high temperatures. *Galileo* and ground-based AO images confirmed these high temperatures. Io's lava is primarily silicate in composition.

Generally, only observations at high spatial resolution can detect the highest surface temperatures present because such high temperatures usually occupy only a small fraction of surface area due to rapid cooling. Moreover, blackbody thermal emission from these high temperatures peaks at short near-infrared wavelengths (the peak of the blackbody curve at ~2,000 K is at ~1.5 μm; at 1,500 K, it is near ~2 μm), requiring measurements at these wavelengths and (ideally) bracketing the emission peak to place robust temperature constraints. There have been two suggestions of ultramafic eruption temperatures on Io: one at Pillan (McEwen et al. 1998, Davies et al. 2001) and the more recent 201308C outburst eruption (de Kleer et al. 2014) (**Figure 1**). It may be possible to differentiate between basaltic and ultramafic lavas from temperature derivation alone if the style of eruption generates a distribution of temperatures that is very high while also covering a large area, such as in the case of lava fountaining, or isolates such a high-temperature area through a lava tube skylight (Davies et al. 2016).

3.2.2. Modeling eruption progression. The strongest temperature constraints are possible when eruptions are detected at their onset over a range of wavelengths. When an eruption takes place, the highest temperature areas are often found at the main vent. Then (broadly speaking) as lava flows across Io's surface, heat loss results in formation of an insulating crust that thickens with time. From an observational perspective, a broad wavelength coverage sensitive to the entire temperature range present is required to understand an evolving volcanic system as a whole (see Davies et al. 2010, figure 7*a*). Spectra of an evolving eruption can be simulated using a cooling lava flow model (Carr 1986, Davies 1996, Howell 1997), which models the evolving distribution of surface temperatures as flows spread and surfaces cool. For example, the Io Flow Model (Davies 1996) has been widely used to interpret data and allows for varying compositions, crack fraction,

and variable discharge rate profiles. However, to date it has not been possible to tightly constrain eruption temperature from model fits to data obtained from either spacecraft or ground-based telescopes, as the necessary observations have not been obtained. To do this accurately with telescopes would require fortuitous timing and a very fast telescope response time to make high spatial and temporal resolution observations over a broad range of wavelengths from 0.5 to 10 μm during the peak of a high-volume eruption.

While it remains challenging to determine lava eruption temperature from ground-based observations due to spatial resolution limitations, the style of eruption—the manner in which lava is discharged—can help identify those eruption processes that present the best opportunities for accurate derivation of eruption temperature. Eruption style can be inferred from the ratio of the 2 μm versus 5 μm radiant fluxes ($F_{2/5}$), shown in **Figure 5**, in combination with the radiant flux density (the radiant energy per unit area of the emitting surface) (Davies et al. 2010). The high-energy, high-temperature end-member $F_{2/5} \gtrsim 1$ includes lava fountains, which were observed

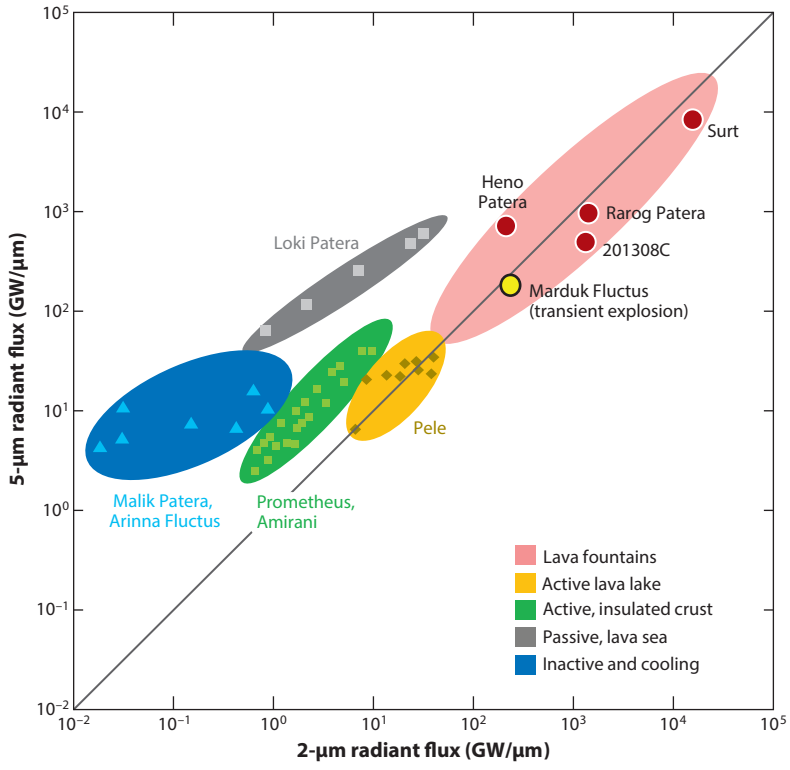

Figure 5

Different styles of eruptions observed on Io span many orders of thermal emission and can be broadly constrained by plotting 2- and 5-μm spectral radiances (Davies et al. 2010) as a proxy for comparing the integrated thermal emission spectra. This figure shows how different styles of activity group together. The most powerful events, outburst eruptions, fall into the red area. Active, overturning lava lakes group into the orange area. Active lava flows, dominated by a relatively cool crust but including a small hot component, fall into the green area. Cooled silicate and possibly sulfur flows and lakes fall into the blue area. The gray area is Loki Patera, which exhibits a unique surface temperature distribution and temporal evolution (Section 3.4). Some notable or typical events are indicated. Base figure modified from Davies et al. (2010), with additional data from de Pater et al. (2014), de Kleer et al. (2014), and Davies et al. (2018).

erupting from long fissures on Io by *Galileo* (Keszthelyi et al. 2001) as well as within the Pele lava lake (Davies et al. 2001). In ground-based observations, recent examples of presumed lava fountaining are the outburst eruptions at Surt (Marchis et al. 2002), Rarog (and likely Heno) Patera (de Pater et al. 2014), and 201308C (de Kleer et al. 2014). All of these events, and others, exhibited large radiant flux densities (kW/m^2) and 2:5 μm radiant flux ratios expected of events dominated by the exposure of large areas at high temperatures. In terms of the integrated thermal emission, these eruptions are the most powerful ever witnessed. The 2001 Surt outburst emitted 78 TW at its peak, almost equivalent to the thermal emission from all of Io, volcanoes included (Marchis et al. 2002).

When an eruption is monitored over days to weeks, or longer, and if a lava flow thickness is measured or assumed, it is possible to determine both the effusion rate (the instantaneous volumetric magma discharge rate) and the eruption rate (the time-averaged discharge rate), leading to an estimate of how much lava was emplaced during the eruption. A typical thickness for highly voluminous outburst eruptions appears to be about 10 m, the approximate thickness of the lava flows emplaced at Pillan in 1997 (Williams et al. 2001). Assuming a final flow thickness of 10 m, analysis of telescope observations of the powerful Rarog and Heno Paterae eruptions in 2013 yielded peak effusion rates of order 10^5 m^3/s. These rates are comparable to the effusion rates at the most energetic eruptions on Earth, such as Mt. Pinatubo in 1990 over a 0.4-h period (de Pater et al. 2014). Most terrestrial eruptions, though, are typically orders of magnitude less. Thinner flows (~1 m) were inferred for more common, lower effusion rate eruptions (Davies et al. 2000), similar to terrestrial basalt lava flows common in Hawai'i.

In several cases, a sequence of large eruptions occurred in the same general area on Io (de Pater et al. 2014, 2016; de Kleer & de Pater 2016b) suggestive of some connectivity between the sites, either through linked magma supply at depth or possibly through seismic shaking from eruptions. Although the data on Io are too sparse to allow a statistical confirmation of such an effect, on Earth eruptions triggering one another have been claimed at separations up to hundreds of kilometers (e.g., Linde & Sacks 1998).

3.3. Spatial Distribution of Io's Geology and Volcanic Heat Flow

Io's geologic features and volcanic heat flow are not randomly distributed. Numerous studies have found that Io's volcanic centers, hot spots, mountains, and some other features are distributed across Io's surface with characteristic—albeit poorly understood—global patterns (e.g., Kirchoff et al. 2011, Hamilton et al. 2013, Keane et al. 2018, de Kleer & de Pater 2016a). These spatial distributions are expected to relate to how and where tidal heat is dissipated in its interior (Section 2.3).

The spatial distribution of the heat flow was derived observationally from *Galileo* Near Infrared Mapping Spectrometer (NIMS), PPR, and Solid State Imaging (SSI) experiment observations of hot spots and dark-floored paterae and flows (250 in total) (Veeder et al. 2012, 2015) and from ground-based AO observations of 75 distinct hot spots (de Kleer & de Pater 2016b, Cantrall et al. 2018, de Kleer et al. 2019b). This integrated collection of hot spots is shown in **Figure 3*a***, alongside end-member models for tidal heating (**Figure 3*b–d***). There is excellent agreement between the *Galileo*-derived and ground-based hot spot distributions. Ground-based observations continuously reveal new volcanic eruptions. About a quarter of the hot spots detected in ground-based AO data from 2001 through 2018 were not previously detected by spacecraft, and some of these have no corresponding surface feature, suggestive of activity only recently initiated at these locations (de Pater et al. 2016, Cantrall et al. 2018, de Kleer et al. 2019b). The increased database provides better statistics on the spatial distribution of hot spots, necessary information for modelers to explain the inner workings of this satellite.

Volcanic features are observed globally but appear to be most frequent at mid-latitudes and in two regions shifted eastward from the sub-/anti-Jupiter points by ~30°, with a relative lack right at equatorial latitudes. While the number of hot spots and cumulative near-infrared radiance are nearly identical between the leading and trailing hemispheres, bright transient eruptions usually take place on the trailing hemisphere (de Kleer et al. 2019b) and at preferentially higher latitudes (de Kleer & de Pater 2016a, Cantrall et al. 2018). Mountains are also observed globally (although they are less numerous than volcanic features) and appear to be anticorrelated with volcanic features at global scales, favoring slightly higher latitudes and being clustered in regions slightly eastward of the leading/trailing point (90°W and 270°W, respectively). This anticorrelation breaks down at local scales, where volcanic features and mountains are often seen in close association. The origin of these long-wavelength patterns is still uncertain. The leading hypothesis is that these patterns reflect patterns of tidal heating at depth, with different patterns arising from dissipation in different layers (Tackley et al. 2001, Hamilton et al. 2013, Tyler et al. 2015, de Kleer et al. 2019d) (**Figure 3*b–d***). The observed distribution of Io's hot spots (**Figure 3*a***) is not well matched by any single end-member tidal heating model (**Figure 3*b–d***). Past research has relied on combinations of different models—for example, dissipation in both the asthenosphere (to explain low-latitude heat flow) and the mantle (to explain high-latitude volcanism)—with mixed results (Hamilton et al. 2013, Davies et al. 2015). Other hypotheses to explain the volcano distribution include convection (Schenk et al. 2001, Tackley et al. 2001), or feedbacks between volcanic eruptions and lithospheric stress (McKinnon et al. 2001, Kirchoff & McKinnon 2009, Bland & McKinnon 2016, Kirchoff et al. 2020), and tidal stresses (Ahern et al. 2017). The mismatch between current tidal heating models and the observed volcano distribution may be improved by more advanced modeling (Section 2.3) or may reflect that the distribution of volcanic thermal emission is not set by the spatial distribution of heat flow in Io's interior.

As mentioned in Section 1, volcanic hot spots can account for only about half of Io's heat flow. The other half is distributed across the rest of Io, possibly preferentially in the polar regions (Davies et al. 2015) in the form of hard-to-detect low-temperature thermal sources or conducted to the surface from volcanic intrusions (Veeder et al. 2012).

3.4. Loki Patera

Of all of Io's hundreds of volcanoes, none is more compelling, or more enigmatic, than Loki Patera. *Voyager* images show Loki Patera (309°W, 13°N) as a large patera ~180 km across with a dark, horseshoe-shaped floor around a brighter, cooler island (**Figure 1*c***; insets in **Figure 6**). Ground-based and spacecraft data over the past 40 years have shown that Loki Patera is the most powerful persistently active volcano on Io, although plumes have never been detected above the patera. Its hot lava contributes on average 9% of Io's total thermal emission (Matson et al. 2006, Veeder et al. 2015). It is still a mystery how Loki Patera can supply the large lava volume—100 km^3/year, according to Matson et al. (2006)—needed to produce the observed thermal emission through solidification and cooling. Another subject of debate concerns the mechanism of renewal of the dark patera floor. Is Loki Patera a massive lava lake, or is the floor of the patera frequently resurfaced with lava flows? Matson et al. (2006) examined the different likely resurfacing mechanisms at Loki Patera and concluded that, from a physical standpoint, resurfacing with lava flows would not produce the observed temperature and area distributions seen by *Galileo* NIMS (Davies 2003) over a large part of the patera floor. High-resolution *Galileo* imagery did not reveal any individual surface flows within Loki Patera but did observe a specular reflection from a flat, likely glassy surface, showing no edifices built up on the floor of the patera (Geissler et al. 2004a). While not conclusive, this flatness was more in keeping with the crust on a lava lake rather than resulting from lava flows.

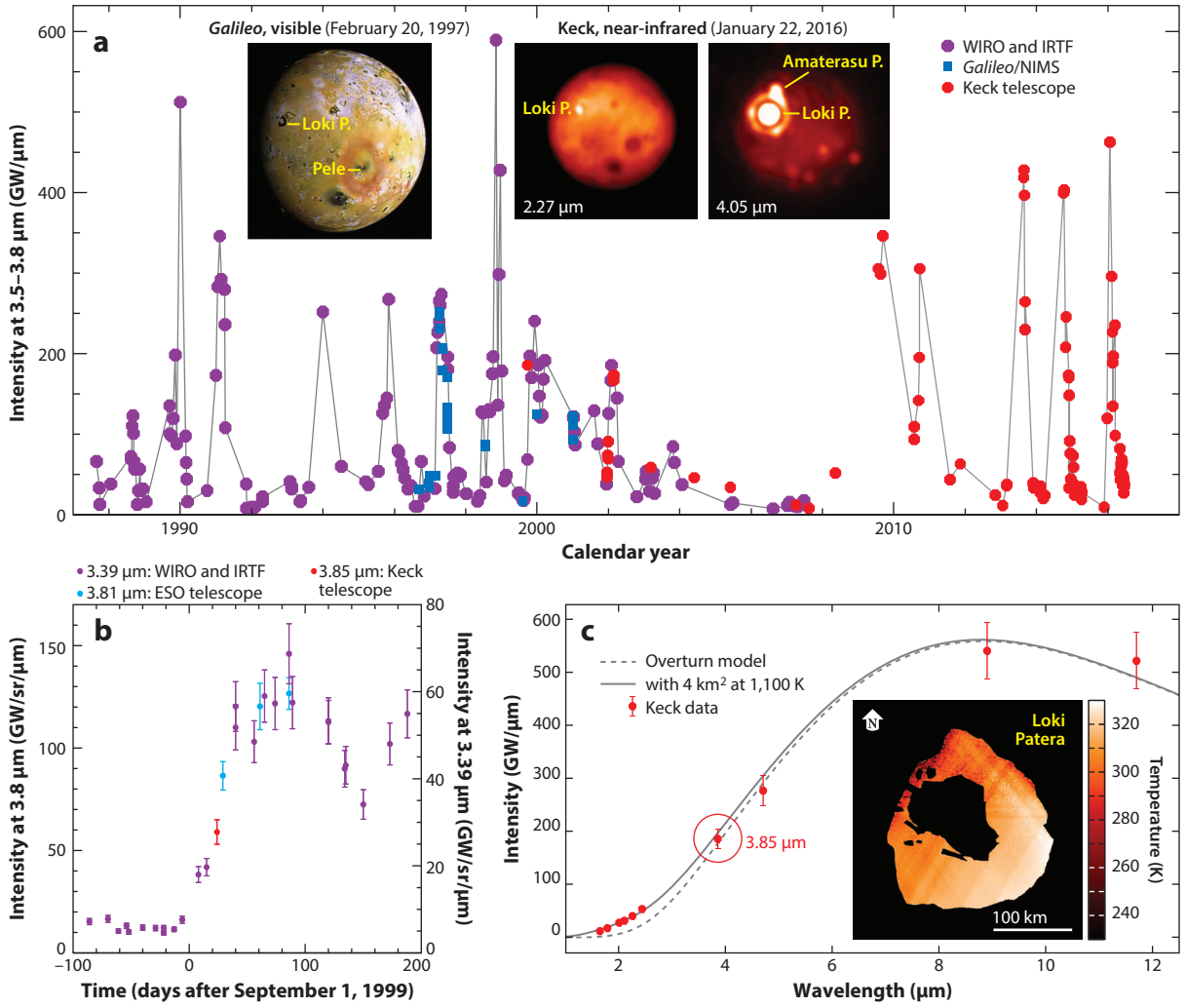

Figure 6

(*a*) Timeline of Loki Patera observations at a wavelength of 3.5–3.8 μm, obtained by different observers, telescopes, and spacecraft. Insets are a visible-light *Galileo* image, with Loki Patera and Pele indicated, and two near-infrared images taken with the Keck telescope during a brightening event. Note that emission is visible at 2.27 μm during such events. Purple dots indicate data from WIRO and the IRTF (Rathbun et al. 2002, Rathbun & Spencer 2006). Blue squares indicate data from *Galileo*/NIMS (Davies et al. 2012). Red dots are from the Keck telescope (de Pater et al. 2017; de Kleer & de Pater 2016b, 2017). Details are in figure 8 of de Pater et al. 2017. (*b*) A timeline of the 1999 brightening event, using data from Howell et al. (2001) (*purple* and *light blue circles*), and the 3.85-μm data point circled in panel *c* from September 24, 1999 (in *red*) (de Pater et al. 2017). (*c*) Spectrum from September 24, 1999, superposed with the overturning lava lake model (*dashed line*; see text). The solid line shows the same model, including a high-temperature (1,100 K) component, covering an area of 4 km^2, to fit the short-wavelength part of the spectrum. (*Inset*) Temperature map of Loki Patera as derived from occultation light curves obtained with the Large Binocular Telescope Interferometer when Europa passed in front of Io (see text). The outline of the patera and the cool central island are fixed based on spacecraft imaging data, and the intensity distribution is determined by fitting a model to the occultation light curve. Abbreviations: ESO, European Southern Observatory (Chile); IRTF, InfraRed Telescope Facility (Hawaii); WIRO, Wyoming Infrared Observatory. Panels *a–c* adapted with permission from de Pater et al. (2017); panel *c* inset adapted from de Kleer et al. (2017).

The long timeline of Loki Patera observations at ∼3.8 μm shown in **Figure 6*a*** reveals a periodic pattern of brightenings with peak intensities over 400 GW/μm (Rathbun & Spencer 2006, de Pater et al. 2017); its 420- to 540-day period roughly matches the timescale on which Io's eccentricity is varying due to perturbations from the other moons, although whether there is a causal relationship remains unconfirmed (de Kleer et al. 2019c).

The brightening episodes are most simply explained if Loki Patera is an overturning lava lake (Rathbun et al. 2002), where the small variations in the interval between brightenings depend on the magma properties, such as temperature and porosity (Matson et al. 2006, de Kleer & de Pater 2017). de Kleer & de Pater (2017) also show that observations at different emission angles are suggestive of topographic shadowing due to a wall or edge surrounding the lake. When matching Loki Patera's 1.5–12-μm spectrum (**Figure 6*c***) with the overturning lava lake model during a brightening episode (**Figure 6*b***), the short-wavelength data revealed a small area, or distributed cracks, covering ∼4 km^2 with temperatures of ∼1,100 K (de Pater et al. 2017), confirming the presence of a small high-temperature emitting area as inferred from *Galileo*/NIMS data (Matson et al. 2006). Finally, in contrast to energetic eruptions where a hot spot brightens very fast (perhaps minutes or hours), a brightening of Loki Patera happens gradually, over ∼50 days, and stays bright for another ∼60 days (Howell et al. 2001, de Kleer & de Pater 2017).

The concept of replacement of crust on a lava lake by foundering was bolstered by observations during the *Galileo* era that showed that the area of greatest thermal emission moved around the south side of the lake in an anticlockwise direction (Spencer et al. 2000, Macintosh et al. 2003, Davies 2003). This direction, though, had reversed by 2009 (de Pater et al. 2017), and images obtained with the Large Binocular Telescope Interferometer (LBTI) showed two bright spots on the south side of Loki Patera (Conrad et al. 2015) (**Figure 1*c***). However, subsequent LBTI observations were to prove crucial in understanding what was happening within Loki Patera. de Kleer et al. (2017) observed Io with the LBTI when Europa passed in front of the satellite on March 8, 2015. Using the 4.8-μm light curve of Loki Patera as it was occulted by Europa and as it reappeared, the authors derived temperature and lava surface age maps at an unprecedented spatial sampling of about 2 km over the entire patera (see inset in **Figure 6*c***). The temperature map is indicative of a multiphase resurfacing process in which two crust founderings propagated around the patera to the north and south of Loki Patera's central island, moving from west to east, and converging to the east of the island. de Kleer et al. (2017) found different velocities and start times of these waves, which are attributed to variations in the lava gas content and/or crust bulk density across the patera. This interpretation reconciles the apparent problems with previous analyses that used only one foundering event on a specific part of the lava lake.

4. IO'S ATMOSPHERE

The first evidence for the existence of an atmosphere on Io was obtained in 1973, when the *Pioneer 10* spacecraft detected ionospheric layers above Io's surface near its terminator (Kliore et al. 1974). Six years later, *Voyager 1* discovered plumes above Pele and Loki (a lava flow field just to the northeast of Loki Patera), which was the first evidence of volcanic activity on a body other than Earth (Morabito et al. 1979). It confirmed the Peale et al. (1979) prediction of such activity made just prior to the flyby. In addition to the visible plume, Pearl et al. (1979) identified the presence of SO_2 gas from an analysis of 7.3-μm spectra of Loki. However, it was not until a decade later that Io's global SO_2 atmosphere was observed, using the Institut de Radioastronomie Millimetrique (IRAM) telescope at 1.4 mm (222 GHz) (Lellouch et al. 1990, 1992). These data revealed a surface pressure of order 4–40 nbar (column densities of 2×10^{17} to 2×10^{18} cm^{-2}). The emission line profiles were saturated and indicated that only a fraction of Io's surface (3–20%) was covered by an atmosphere, with a temperature of order 500–600 K.

4.1. Observational Methods

Since those early detections, Io's SO_2 atmosphere has been observed at more millimeter-wavelength transitions, as well as in the UV, near-, and mid-infrared. All techniques have their advantages and shortcomings:

1. Millimeter: At millimeter wavelengths, one detects thermal emission from the atmosphere, typically 20–40 K above the background (subsurface) temperature (~90 K) (Section 3.1) for disk-integrated data. The emissions occur in local thermodynamic equilibrium (LTE) (Lellouch et al. 1992)—i.e., the atmospheric temperature determines which energy levels in the molecule are populated via the Boltzmann equation. Hence, by observing different transitions, one should, in principle, be able to determine the temperature, column density, and fractional coverage of the atmosphere. However, in practice most observable transitions have similar (low) energy levels, which to date has precluded accurate temperature measurements. Moreover, the interpretation of line shapes, indicative of temperature, may be complicated by winds (Section 4.3).
2. Ultraviolet: At UV wavelengths, Io is seen in reflected sunlight, and both SO_2 gas and surface frost absorb strongly. It is difficult to disentangle the surface and atmosphere contributions, in part because the absolute surface reflectance depends strongly on unknown properties such as grain size and how the frost is mixed in with other components. Dust absorbs strongly at these wavelengths as well, and may affect the analysis. High spectral resolution is required to distinguish gas absorptions from surface frost; off-limb observations of Io transiting Jupiter have also been used to remove contamination from Io's surface, but require high spatial resolution in the UV/optical (Spencer et al. 2000). The atmospheric absorption features are primarily sensitive to the column density of the gas, although the band contrast decreases somewhat with increased temperature (Wu et al. 2000).
3. Mid-infrared: SO_2 vibration/rotation lines in the mid-infrared (ν_2-band at 19 μm, ν_3-band at 7.3 μm) will be seen in emission if the vibrational temperature is higher than the surface temperature and in absorption if it is lower. Since the lines are seen in absorption while the atmosphere is warmer than Io's surface, non-LTE effects must be important. Indeed, at the low atmospheric density, the collisional timescales are longer than the radiative timescales, and the absorption depth of the lines is affected by radiative exchanges with the surface and deep space (Lellouch et al. 1992) in addition to the expected dependence on atmospheric temperature, density, and surface temperature.
4. Near-infrared: The $\nu_1 + \nu_3$ band at 4.0 μm is located in the dominantly solar-reflected part of Io's spectrum. It is seen in absorption (like in the UV) and is not subject to non-LTE effects (Lellouch et al. 2015). The absorptions are rather faint, however, and can only be observed using an instrument with both high sensitivity and high resolving power.

4.2. Atmospheric Models

Over the past decades, models have been developed to explain particular aspects of Io's atmosphere, such as its vertical, longitudinal, and latitudinal structure including winds; its thermo- and photochemistry; and its interactions with the plasma torus. No single model exists as of yet that couples these various aspects.

Models of Io's atmospheric temperature include sublimation equilibrium (also referred to as buffered) models originally developed by, for example, Fanale et al. (1982) and Kerton et al. (1996). More recently, 3D simulations have been conducted using a Monte Carlo method, with ever-more-realistic physical processes (Moore et al. 2009; Walker et al. 2010, 2012). In the most recent

of these models, Walker et al. (2012) first constrain Io's thermophysical properties [albedo and thermal inertia (Section 3.1)], assuming fixed areas on the surface covered by SO_2 frost and non-frost and including about two dozen hot spots. They solve the 1D heat conduction equation with depth into Io's surface, including effects of eclipses, radiation from Jupiter, and latent heat of sublimation and condensation. The thermophysical parameters are then used as boundary conditions in 3D simulations of Io's sublimation-driven atmosphere, including plasma heating, daily solar eclipses, and atmospheric dynamics (e.g., winds).

Zhang et al. (2003, 2004) developed an elaborate model for volcanic plumes including a full treatment of gas dynamics (Monte Carlo simulations of the plume expansion and reentry shock), entrained particulates, radiation (heating and cooling through rotational and vibrational radiation), sublimation, and condensation. McDoniel et al. (2017) coupled this plume model to that of a sublimation-driven atmosphere to show how a volcanic plume expands in an atmosphere.

Atmospheres can also be created through sputtering on the surface when energetic magnetospheric particles impact a satellite's surface, as reviewed by Cheng & Johnson (1989). For ions to reach the surface, the atmospheric column density must be $\lesssim 10^{16}$ cm^{-2}. Hence, contributions to the atmosphere through sputtering can be expected only at locations with a tenuous or no atmosphere, such as at high latitudes, or when the satellite is in eclipse (or at night).

Strobel et al. (1994) developed a model of Io's vertical thermal structure by solving the 1D heat balance equation over time, including solar heating in the UV and near-infrared bands of SO_2, plasma, and Joule heating, as well as radiative losses due to non-LTE cooling by rotational and vibrational lines of SO_2. Summers & Strobel (1996) added photochemistry to evaluate in particular O_2, SO, and SO_2 altitude profiles for different eddy diffusion coefficients. Moses et al. (2002a,b) included volcanic sources in photochemical models, using thermochemical calculations of the composition of volcanic gases exsolved from the magma by, for example, Fegley & Zolotov (2000) and Zolotov & Fegley (2000). The eruption temperatures in these models are assumed to be high enough that volcanic gases are in chemical equilibrium near the vents but may be quenched in the cooling expanding plumes. Schaefer & Fegley (2004, 2005) improved the above models to study the vaporization of lavas on Io in chemical equilibrium over a wide range of temperatures and pressures, for different silicate compositions.

4.3. The Bulk SO_2 Atmosphere: The Product of Outgassing or Sublimation?

Based on a variety of observations of SO_2 gas, several authors have argued that Io's atmosphere is, at least partially, driven by sublimation, whereas others argue in favor of volcanism. Disk-integrated observations from the UV to millimeter wavelengths all consistently show larger column densities on the anti-Jovian (180°W) hemisphere ($\sim 10^{17}$ cm^{-2}) than on the sub-Jovian (0°W) hemisphere ($\sim 10^{16}$ cm^{-2}) (e.g., Spencer et al. 2005, Feaga et al. 2009). Variations in column density are $\lesssim$30% and seemingly uncorrelated with hot spot activity (Roth et al. 2020). Using mid-infrared data from 2001 to 2010, Tsang et al. (2012) show that the SO_2 abundance increases with decreasing heliocentric distance, as expected for a sublimation-driven atmosphere.

Disk-resolved data at UV wavelengths from *HST* over multiple years reveal that SO_2 is mainly confined to latitudes within 30°–40° from the equator, with a larger latitudinal extent on the anti-Jovian side (Feaga et al. 2009). The latter data further show that the highest column densities are at longitudes between ∼120° and ∼180°, which corresponds well with the presence of the thickest SO_2 frost coverage as determined from SO_2 ice maps at 2.12 μm (Laver & de Pater 2009, de Pater et al. 2020a) (**Figure 2*c***). While the decreasing insolation at higher latitudes inhibits SO_2 sublimation, Feaga et al. (2009) suggest that the longitudinal asymmetry is caused by an asymmetry in volcanic sources. Such a scenario requires a maximum in volcanic sources in the 120–180°W

range, which is not supported by the observed distribution of volcanic thermal emission (e.g., Cantrall et al. 2018, de Kleer et al. 2019b) (Section 3.3).

Using their sublimation model, Walker et al. (2012) determined a slightly higher surface temperature on the anti-Jovian side than the sub-Jovian hemisphere due to the daily 2-h eclipses. This results in a higher SO_2 abundance on the anti-Jovian side because the vapor pressure is a steep exponential function of temperature ($P_{vapor} = 1.52 \times 10^8 e^{-4510/T}$ bar) (Wagman 1979).

The longitudinal asymmetry, confinement to low latitudes, and rather constant SO_2 abundances over time are consistent with an atmosphere being supported by sublimation of SO_2 ice. Interpretation of several other data sets, including SO_2 maps at millimeter wavelengths obtained with the Submillimeter Array (SMA) (Moullet et al. 2010), also favors a sublimation-driven atmosphere. However, SO_2 gas is enhanced above some volcanic hot spots (McGrath et al. 2000), and Pele's plume contains the sulfur-rich gases S_2, S, and SO (McGrath et al. 2000, Spencer et al. 2000, Jessup et al. 2007), indicative of volcanic contributions to Io's atmosphere.

4.3.1. Eclipse observations. Observations of Io right before, after, and during an eclipse provide the best way to separate the volcanic from sublimation-driven contributions (at least when restricted to Earth-based viewing geometries). The atmospheric temperature is expected to drop within minutes after Io enters an eclipse (de Pater et al. 2002). The SO_2 gas that makes up the bulk of Io's atmosphere is expected to condense out on a similar timescale, dictated by the vapor pressure of the gas, unless a layer of noncondensible gases prevents rapid collapse (Moore et al. 2009).

Tsang et al. (2016) obtained the first direct observations of the 18.9-μm SO_2 ν_2-band in Io's atmosphere with the Texas Echelon Cross Echelle Spectrograph instrument on the Gemini telescope while the satellite entered an eclipse. They measured a steep drop in surface temperature within minutes after entering eclipse (**Figure 7*a***). A range of atmospheric cooling models suggest

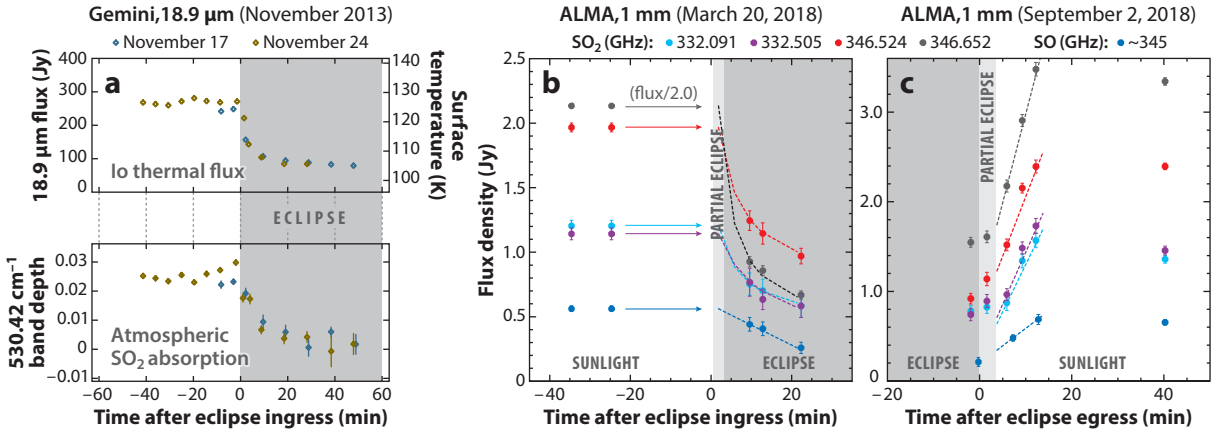

Figure 7

Observations of Io going into and emerging from eclipse. (*a*) Gemini data at 18.9 μm: (*top*) the thermal flux of Io and (*bottom*) the SO_2 absorption depth at 530.42 cm^{-1} on November 17 and 24, 2013, as a function of time relative to eclipse ingress. Panel *a* adapted with permission from Tsang et al. (2016). (*b*,*c*) Atacama Large Millimeter/submillimeter Array (ALMA) data at 1 mm. SO_2 and SO flux densities are plotted as a function of time for eclipse ingress (*panel b*) and egress (*panel c*). The dotted lines superposed on the data in panel *b* show the exponential decrease in the first few minutes after entering eclipse. In panel *c* the dotted lines show the linear increase after emerging from eclipse on September 2. These data are normalized to a geocentric distance of 5.044 AU. Panels *b*,*c* adapted from de Pater et al. (2020b).

that the SO_2 column density simultaneously dropped by a factor of 5 ± 2, suggesting that the atmosphere must contain a large component that is supported by sublimation. In contrast, though, they did not see any change when Io went from eclipse into sunlight, which they attributed to a larger number of active volcanoes near the egress longitudes (~20°W) compared to ingress (~340°W).

The most recent observations contributing to the debate regarding a sublimation versus volcanically driven atmosphere have been obtained with the Atacama Large Millimeter/submillimeter Array (ALMA) in the 1-mm wavelength band, when Io went into and emerged from eclipse (de Pater et al. 2020b). The evolution of the disk-integrated intensities of SO_2 (in several transitions) and SO is shown in **Figure 7*b*,*c***. During eclipse ingress, the SO_2 flux density dropped exponentially, and the atmosphere reformed in a linear fashion when reemerging in sunlight, with extra (up to ~20%) post-eclipse brightening after ~10 min. Disk-integrated in-sunlight flux densities are approximately two to three times higher than in-eclipse, indicative of a roughly 30–50% contribution from volcanic sources; for a purely sublimating atmosphere, the SO_2 flux density in eclipse should have been essentially equal to zero, unless the presence of nonvolatile gases prevents complete collapse (Moore et al. 2009).

The gradual increase in the SO_2 intensity during the first ~10 min upon eclipse egress may explain observations by Binder & Cruikshank (1964), who reported that Io was much brighter in reflected sunlight immediately after eclipse egress than 10–20 min later. To explain their observations, the authors hypothesized the presence of an atmosphere (not known at the time) condensing while in eclipse, and as soon as the surface warmed again, the gas (SO_2) would sublime and with it the satellite's surface would darken again. However, the reality of these observations remains controversial, as subsequent data have not shown this effect (e.g., Secosky & Potter 1994).

Interestingly, the disk-integrated SO_2 column density (1.5×10^{16} cm^{-2}) and temperature (~270 K), derived under the assumption of an atmosphere in hydrostatic equilibrium, appear to be the same for both the Io in-sunlight and in-eclipse data; the difference appears to be mainly caused by a decrease in fractional coverage when in eclipse (de Pater et al. 2020b).

4.3.2. Spatial brightness distribution. **Figure 8** shows images of the spatial distribution of SO_2 on Io when the satellite entered eclipse and during eclipse egress. About 6 min after entering eclipse, the emissions had substantially decreased, and peaks were seen near the volcanic sites Karei and Daedalus Paterae. The only emissions visible 10 min later were from near these two volcanoes and North Lerna. In September, right before exiting eclipse, a volcanic plume was visible on Io's limb near P207, a small, visibly dark patera where plumes had not been seen prior to these ALMA observations. As soon as sunlight hit the satellite, SO_2 emissions became stronger, in particular in the regions where volcanic plumes were present during eclipse, and after ~10 min, the atmosphere had completely reformed (de Pater et al. 2020b).

Figure 9 shows a series of ALMA images at different velocities for the in-sunlight SO_2 data. This series of images reveals that the strong emission above P207 is the only feature visible at radial velocities of almost ~−0.8 km/s (frame 1), and it dominates the emission at approximately +0.4 km/s in frame 3. Clearly, these volcanic plumes shape the high-velocity wings of the disk-integrated line profile (frame 4). In frame 1 the gas is moving toward us—i.e., presumably the front side of the umbrella-shaped plume—and in frame 3 we see the back side of the canopy moving away from us.

4.3.3. Comparing plume models with observations. In the following section, we compare the ALMA data with model simulations of a plume on the night and day sides. During eclipse, a large gaseous plume can be compared with the night side Pele plume modeled by Zhang et al.

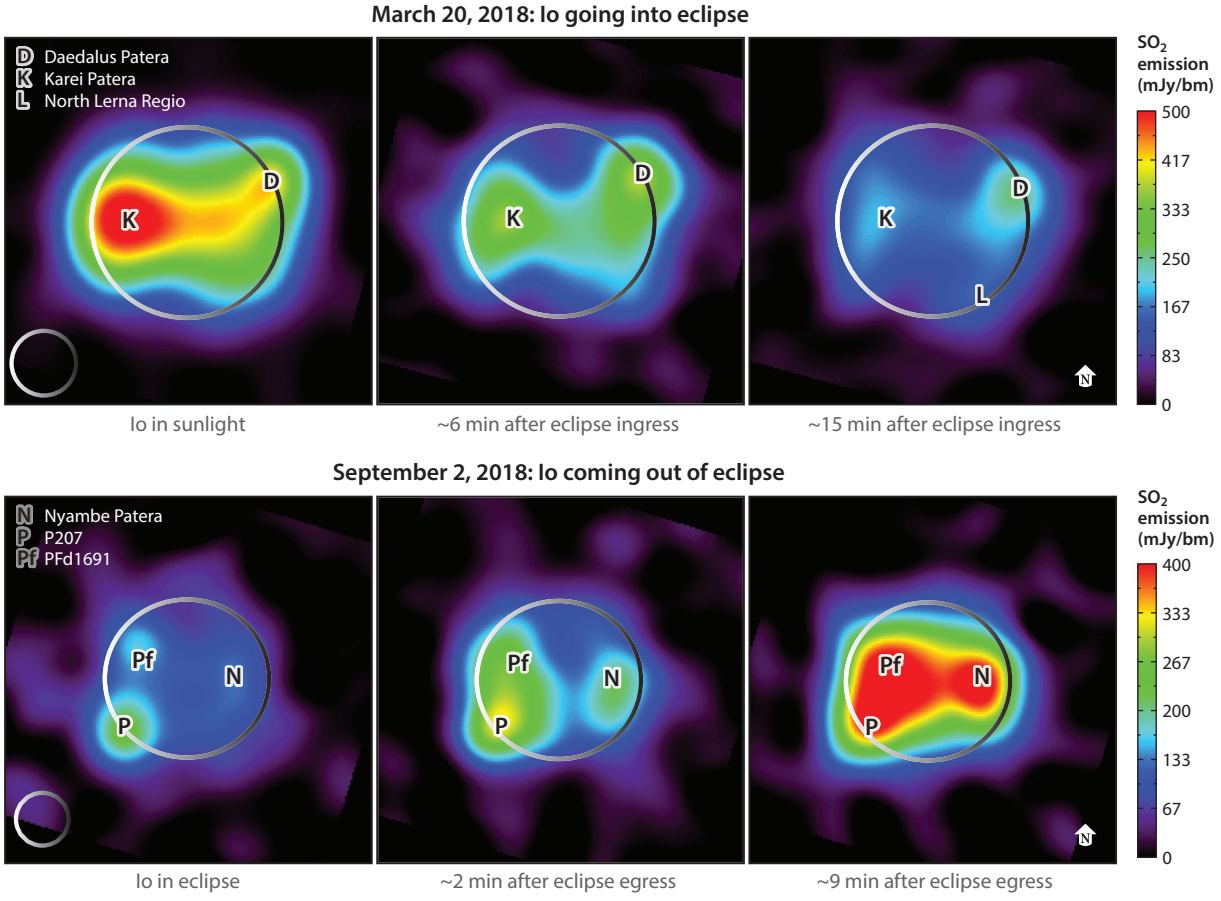

Figure 8

Individual frames of a series of Atacama Large Millimeter/submillimeter Array (ALMA) SO_2 maps constructed from data at 346.652 GHz when Io went into eclipse (March 20, 2018) and emerged from eclipse (September 2, 2018). The data are averaged over 0.4 km/s (~0.45 MHz). The large circle shows the outline of Io, and the small circle in the lower left shows the resolution of the data (0.35" or 1205 km in March; 0.30" or 1235 km in September). The effect of volcanoes on Io's SO_2 emission is clearly seen. Figure adapted from de Pater et al. (2020b).

(2003). In this model, the gas erupts from the vent at a temperature of 650 K and a source rate of ~10^{29} SO_2 molecules/s at hypersonic velocities of ~1 km/s. It then expands and cools. At an altitude of ~300 km, a canopy-shaped shock forms (due to Io's gravity field) where the radially expanding molecules turn back down to the surface, as shown in **Figure 10*a***. Most of the gas falls down ~400–600 km from the vent, where it condenses and forms a ring around the volcano—i.e., matching the red ring observed around Pele (e.g., **Figure 2*a***; inset **Figure 6*a***).

During the first few minutes after eclipse egress, the plume transitions from a night side plume to one on the day side, where SO_2 sublimation from SO_2 frost becomes important. The plume starts to interact with the subliming atmosphere, as shown for a large plume at 30°N latitude in **Figure 10*b–d*** (McDoniel et al. 2017). The extent to which a day side sublimation atmosphere is affected by plumes depends on the size, density, and ejection velocity of the plume, as well as on the density of the sublimation atmosphere, which is set by the vapor pressure curve in the atmosphere. A large Pele-type plume will rise well above the exobase [which is typically at ~30

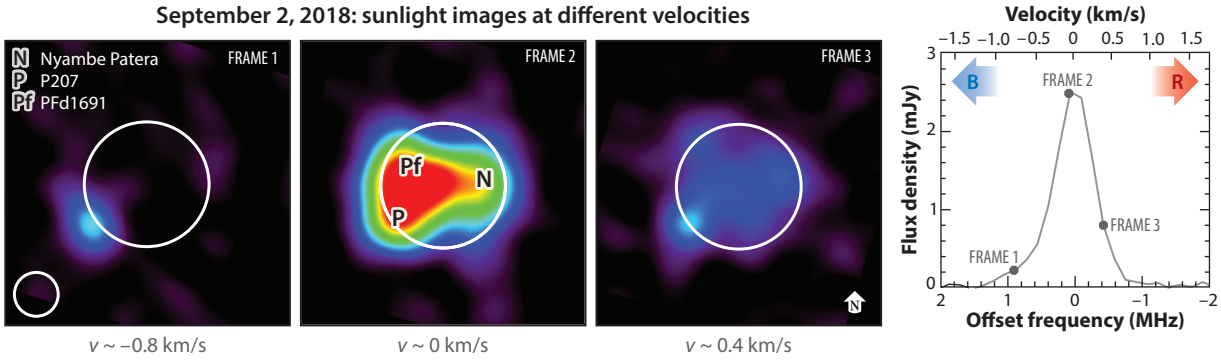

Figure 9

Individual maps at different offset frequencies (velocities), like frames from a movie, obtained with the Atacama Large Millimeter/submillimeter Array (ALMA) on September 2, 2018, when Io was mapped while in sunlight. Data at two transitions (346.652 and 346.524 GHz) were combined to increase the signal-to-noise ratio. Each frame is averaged over 0.142 km/s (~0.16 MHz), and the line is centered on Io's frame of reference. As in **Figure 8**, the large circle shows the outline of Io, and the small circle shows the resolution of the data. The fourth panel shows the disk-integrated line profile, and the gray dots indicate the offset frequency (velocity) of each map (i.e., frames 1–3). The symbols B (blueshift) and R (redshift) show the velocities of gas moving toward (B) or away (R) from us. The rotation of Io causes the west limb (*left side*) to move toward us and the east limb away from us; the asymmetry of the line is caused by the high gas velocities in the volcanic plume. The approximate positions of several volcanoes are indicated on frame 2. Figure adapted from de Pater et al. (2020b).

to 50 km (McDoniel et al. 2017)] and produce a canopy shock similar to that on the night side (**Figure 10*a***). However, whereas at night the gas falls down and impacts the surface, during the day it will encounter the atmosphere. A reentry shock develops, heating the gas up to levels similar to those seen above the vent. While the high temperature will lead to excess frost sublimation, the high pressure will push material away, which results in a depression in the column density at the intersection of the canopy, shown in **Figure 10*c*,*d***. McDoniel et al. (2017) show calculations of a plume transitioning from the night to the day side, and back into the night, a process that takes almost a full Io day (42.5 h). The ALMA observations, in contrast, show a very accelerated process because eclipse egress takes only a few minutes. The high temperature caused by the reentry shock may lead to a sudden increase in SO_2 emissions, which could explain the overshoot or post-eclipse brightening in the ALMA intensity ~10 min after egress (de Pater et al. 2020b).

The ALMA data show that the SO_2 column densities in volcanic plumes are very similar to those measured over the entire disk, but the fractional coverage in plumes is much higher: ~50%–60% in sunlight, almost twice as large as for the disk-integrated profiles. This is consistent with the plume simulations by Zhang et al. (2003) and McDoniel et al. (2017), who show that during the day the column density over the plume matches that over the day side hemisphere, except over the small area directly over the vent, which is much smaller than the ALMA resolution. McDoniel et al. (2017) show how material from a realistic Pele-type plume can become suspended in a sublimation atmosphere and how it may alter the atmospheric composition while it does not have much effect on its total mass.

However, even though the plume models match the data overall very well, the observed velocity profiles show many asymmetries that suggest that the volcanic eruptions are much more complicated than the models predict. This is not too surprising; volcanic eruptions are likely not axisymmetric and may fluctuate in ejection speed, direction, and gas content on timescales much shorter than can be captured in such observations. The interaction with the sublimation atmosphere, although already complex in the models, may also be even more complex in reality.

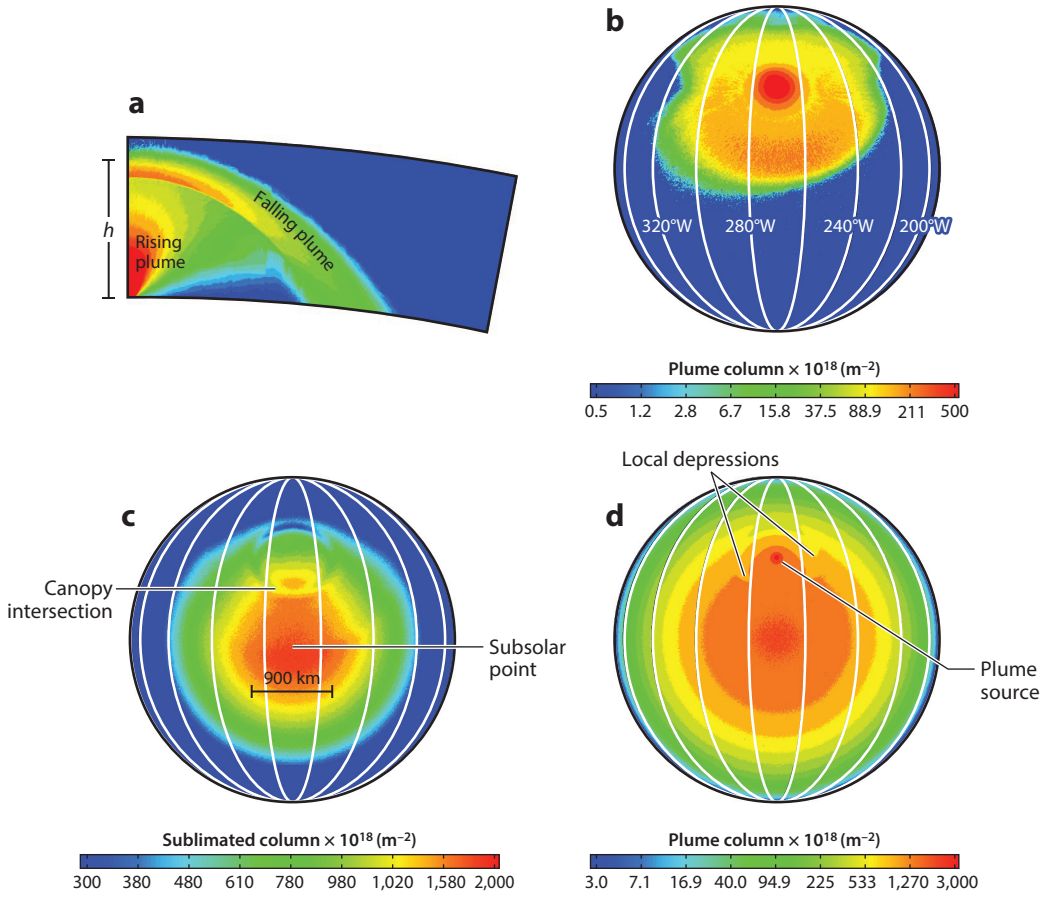

Figure 10

Calculations of the interaction of a plume with the sublimation atmosphere, as seen from the top. Contours of column density are shown for Io's day side with a plume at 30°N; the peak frost temperature is 118 K. (*a*) Sideways view of the plume by itself. (*b*) Column density for SO_2 that erupts from the plume source. (*c*) Column density for SO_2 that sublimates directly from surface frost. (*d*) Total column density of plume in the sublimating atmosphere. Figure adapted with permission from McDoniel et al. (2017).

4.3.4. Atmospheric winds. Moullet et al. (2008) reported a horizontal wind of ∼300 m/s in the prograde direction from IRAM Plateau de Bure maps. Such winds are hard to reconcile with models, which indicate day-to-night winds and local winds away from volcanic vents (Ingersoll et al. 1985, Gratiy et al. 2010). An enhancement in atmospheric SO_2 near the dawn terminator due to molecules desorbed from the warming rock surface (Walker et al. 2010) may imitate a prograde zonal wind; this phenomenon may explain ALMA observations during a period of low volcanic activity (de Pater et al. 2020b).

4.3.5. Atmospheric temperature. One of the largest uncertainties in atmospheric models of Io is the temperature profile. While disk-integrated thermal infrared data of the 18.9-μm ν_2-band of SO_2 showed a temperature of ∼110–115 K (Spencer et al. 2005), interpretation of disk-resolved observations of the SO_2 $\nu_1 + \nu_3$ band at 4 μm favored a temperature of ∼170 K (Lellouch et al. 2015). Analysis of data at (sub)millimeter wavelengths showed temperatures ranging from ∼150 K

up to 320 K (e.g., Moullet et al. 2010, de Pater et al. 2020b, Roth et al. 2020). Although these temperatures show a large spread in values, they all are much lower than the original millimeter-wavelength measurements (500–600 K) and in better agreement with the Strobel et al. (1994) and Walker et al. (2010) models. The latter authors show that the temperature increases from the surface, at essentially the frost temperature, up in altitude due to plasma heating from above, while the gas cools due to vibrational and rotational radiation. The temperature profile is expected to vary with latitude, longitude, and time of day, while the presence of plumes may impact the temperature quite dramatically (Section 4.3.2). Hence, it is perhaps not surprising that disk-averaged observations at different wavelengths, likely probing different regions in the atmosphere, give different results when the atmosphere is assumed to be isothermal and in hydrostatic equilibrium.

Accurate temperature profiles are important for the derivation of column densities for different species and the interpretation of isotopic ratios. For example, Moullet et al. (2013) reported a $^{34}S/^{32}S$ ratio about two times higher than Earth and interstellar medium values. However, without knowing the temperature profile, this ratio is highly uncertain, and we cannot say whether this ratio agrees or disagrees with the terrestrial value.

4.4. Minor Atmospheric Constituents

4.4.1. SO. In an SO_2-dominated atmosphere, photochemistry alone would lead to the formation of SO, S, O, and O_2. SO has been detected at a typical SO/SO_2 ratio of order 0.03–0.10 (e.g., Lellouch et al. 2007). However, it is unclear if SO is produced primarily through photochemistry or directly in volcanic eruptions (Zolotov & Fegley 1998). Based on an analysis of SMA maps (Section 4.3), photolysis of SO_2 was suggested to be the main source of SO because volcanic activity was not sufficient to explain the SO column density and distribution as observed (Moullet et al. 2010). In addition, the SO spatial distribution tracks the SO_2 distribution very well in the ALMA observations discussed in Section 4.3.2.

When entering eclipse, the SO flux density dropped linearly (**Figure 7*b***), and much faster than expected (Moses et al. 2002b), although clearly delayed compared to the exponential drop in the SO_2 intensity. This suggests that SO may be rapidly removed from the atmosphere through reactions with itself on Io's surface (Lellouch 1996, de Pater et al. 2020b). Upon eclipse egress, the SO flux density increased linearly, again delayed compared to SO_2, which provides further support that photolysis of SO_2 is a major source of SO.

In addition to the above millimeter-wavelength observations, SO has also been observed in the near-infrared, at 1.707 μm (de Pater et al. 2002). This forbidden electronic $a^1\Delta \rightarrow X^3\Sigma^-$ transition can be observed only while Io is in eclipse because in sunlight the emission band is swamped by Io's reflected light. With an SO bandshape indicative of a rotational temperature of ~1,000 K, de Pater et al. (2002) concluded that the emission resulted from excited SO molecules directly ejected from the then very active volcano Loki Patera. More recent observations at a high spectral resolution (**Figure 11*c***) indicate the presence of gas at both a low (~200 K) and high (~1,500 K) temperature (de Kleer et al. 2019a). The spatial distribution of SO, shown in **Figure 11*a*** (de Pater et al. 2020a), shows that the correlation with volcanoes is tenuous at best. Moreover, both the spatial distribution and the spectral shape of the SO emission band vary considerably across Io and over time. Based on all the available data, de Pater et al. (2020a) suggest that the emissions are likely caused by a large number of stealth plumes, high-entropy eruptions produced by superheating SO_2 vapor at depth through interaction with silicate melts. Such plumes lack dust or condensates, so that they are invisible in reflected sunlight. The high temperatures present excite any SO molecules before ejection from the vent. The presence of stealth plumes was first suggested by Johnson et al. (1995) to explain the patchy SO_2 atmosphere as observed at UV and millimeter wavelengths (Section 4.3).

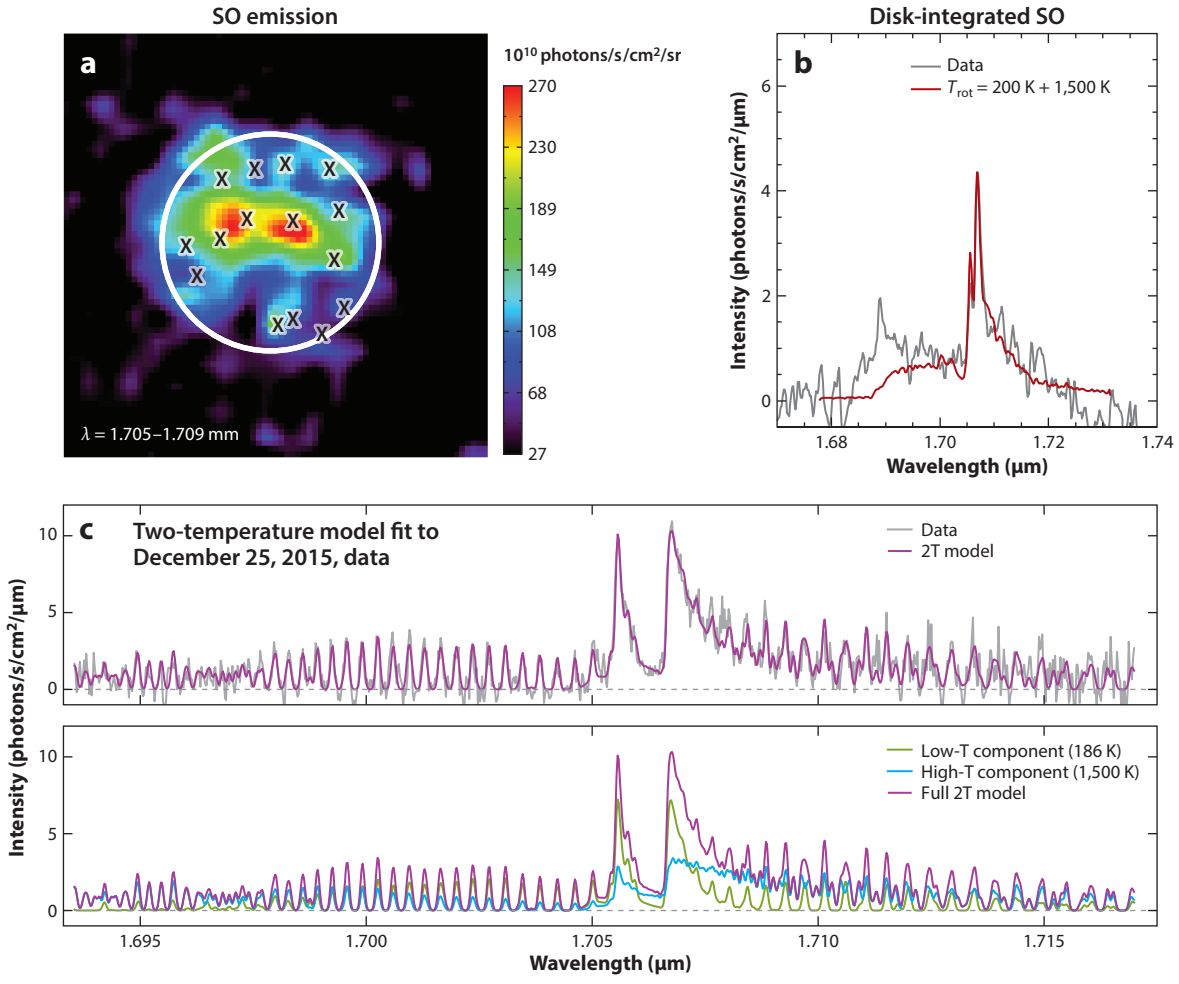

Figure 11

(*a*) Image of the forbidden 1.707-μm emission band of SO obtained with the field-integral OH-Suppressing Infrared Imaging Spectrograph (OSIRIS) on the Keck 1 telescope on December 25, 2015. The image was obtained by integrating over the center channels of the emission band (see *panel b*). Superposed are the location of a number of volcanic centers (note the absence of a clear correlation) and the outline of Io's disk. (*b*) Disk-integrated OSIRIS spectrum of the SO data in panel *a*, with a model consisting of two temperatures (200 and 1,500 K, in approximately equal proportions) superposed. Note that the 1.69-μm feature cannot be matched. (*c*) Disk-integrated spectrum at a high spectral resolving power ($R \sim 25{,}000$) taken simultaneously with the data in panels *a* and *b* using the near-infrared echelle spectrograph on the Keck 2 telescope. A 2-temperature model, very similar to that in panel *b*, is superposed. The individual components of the model are shown in the bottom panel. Panels *a*,*b* adapted from de Pater et al. (2020a). Panel *c* adapted with permission from de Kleer et al. (2019a).

The SO data are further suggestive of non-LTE processes, as shown, for example, by the 1.69-μm feature in the line profile (**Figure 11*b***) that cannot be matched by any LTE model.

4.4.2. S_2, NaCl, and KCl. Other molecules that have been detected in Io's atmosphere are S_2, NaCl, and KCl. S_2 was detected two decades ago from imaging and spectroscopy of Pele's plume on Io's limb against Jupiter (Spencer et al. 2000), at an S_2/SO_2 ratio of 0.08–0.3. Based on thermochemical equilibrium models, this ratio is expected from equilibration with silicate magmas at 1,400–1,800 K.

Gaseous NaCl was first detected by Lellouch et al. (2003), and both NaCl and KCl were mapped with ALMA by Moullet et al. (2015) (maps are displayed in de Pater et al. 2018). The emissions were detected above Isum Patera, but interestingly, no SO_2 emissions were seen at this location, nor have plumes ever been detected above this site. The observed ratio in the flux density, NaCl/KCl, is 4.6, which means that the column abundance ratio, NaCl/KCl, is ∼3–6 for atmospheric temperatures of 150–1,500 K. This is about a factor of three lower than the Na/K ratio in chondrites, and perhaps a factor of two lower than that measured in Io's extended atmosphere (Brown 2001). Because the photochemical lifetime for both species is similarly short [$\lesssim$2 h (Moses et al. 2002a)], they need to be sourced continuously. The difference in the observed versus chondritic ratio may be caused by the fact that KCl has a lower condensation temperature than NaCl (1,173 K versus 1,363 K) and suggests a magma temperature of ∼1,300 K (Fegley & Zolotov 2000). A different set of ALMA observations (de Pater et al. 2020b) showed strong KCl emissions sourced from Ulgen Patera, which at the time did not release detectable SO or SO_2 gas. Nor have plumes ever been detected at this location. Hence, if indeed volcanically sourced, the magma in the chambers that power volcanoes must have different melt compositions, and/or the magma has access to different surface/subsurface volatile reservoirs (de Pater et al. 2020b).

Our knowledge about the alkalis in Io's atmosphere remains very limited. We know that they are highly localized, do not coincide with SO_2, and vary drastically over Io's globe (Redwing et al. 2020), yet column abundances may be stable over time (Roth et al. 2020). Clearly, our understanding of the controls on Io's atmospheric creation and loss is far from complete.

4.4.3. Atomic species. In addition to the formation of SO, dissociation by photon and electron impact in Io's atmosphere results in the atomic species S, O, Na, K, and Cl (**Figure 4**), all of which have been detected in Io's atmosphere and/or in an extended cloud or corona surrounding the satellite (see, e.g., the review by Cruikshank & Nelson 2007). Sulfur was detected in Pele's plume from *HST* data (McGrath et al. 2000). S and O auroral emissions have been detected off the limb along the equator and are attributed to electron impact on the atomic species (Geissler et al. 2004b). In contrast to this earlier work, Roth et al. (2014) show that most of these emissions originate within 100 km from the surface and are very stable over time, indicative of an atmosphere driven primarily by sublimation of SO_2. An observed decrease in these emissions after eclipse ingress and brightening upon egress also supports the sublimation theory. Roth et al. (2014) further show that all variations observed in the auroral emissions can be explained by the local plasma environment and the changing viewing geometry of Io in Jupiter's magnetosphere. The O/SO_2 ratio is 0.10, with an S/O ratio of 0.2 near the surface and ∼0.05 in the corona. Post-eclipse brightening of sodium emissions shows that photodissociation of NaCl accounts for most of the Na produced by Io (Grava et al. 2014).

Ultimately, the various species get ionized and embedded in the Io plasma torus. Charge exchange with such ions leads to fast neutrals, generating the vast sodium cloud surrounding Jupiter that extends to hundreds of Jovian radii (Mendillo et al. 1990). The Japan Aerospace Exploration Agency *Hisaki* satellite has been studying UV emissions from plasma torus ions and neutrals from Earth's orbit since 2013 (Yoshikawa et al. 2014). The resultant data set gives the most extensive view of the torus composition and its spatial and temporal variability to date, and in particular the detailed response of the torus to a volcanic event at Io (Yoshioka et al. 2018). An up-to-date review of Io's space environment by Bagenal & Dols (2019) includes a synthesis of results from *Hisaki*.

5. CONCLUSIONS AND OUTLOOK

Our understanding of Io and the processes at work on/in its surface, atmosphere, and interior has progressed substantially since the *Galileo* era as a result of the observations addressed in this

review. However, many aspects of Io remain poorly understood, and the data obtained over the past 10–20 years have additionally led to new questions. The sidebar titled Outstanding Questions summarizes some of the most pressing scientific questions, and here we describe the outlook for observations to be obtained with new and future ground-based and near-Earth-orbiting telescopes.

OUTSTANDING QUESTIONS

Interior and Geology

1. What are the sizes, compositions, and states of Io's core, mantle, and lithosphere, and does Io have a magma ocean?
2. What is the magnitude and spatial distribution of Io's heat flow, and is it reflected in Io's surface heat flow and geology?
3. Where is tidal heat dissipated within Io (asthenosphere versus deep mantle versus magma ocean), and what are the dissipation mechanisms?
4. What are the compositional range and chemistry of Io's magmas (ultramafic versus mafic versus sulfurous), and is the composition dependent on location?
5. Is Io in thermal equilibrium (heat in equals heat out)?
6. What processes govern Io's heat transport and loss (conduction versus heat-pipe volcanism versus magmatic intrusions)?
7. What is the relationship among topography, volcanoes, mountains, and other tectonomagmatic processes at global and local scales?
8. How do Io's large paterae (such as Loki Patera) form and operate?
9. How long has Io been volcanically active, and is its current level of activity representative?
10. What is the temperature profile and compaction gradient in Io's near-surface, and how does it vary across the moon?
11. How can we reconcile the differences in frost spatial distribution derived from data at different wavelengths and explain the apparent absence of ice at high latitudes?

Atmosphere

1. Is Io's atmosphere primarily supported by sublimation of SO_2 frost or maintained dynamically by volcanic eruptions?
2. What happens at night (or during an eclipse)—that is, how much of Io's SO_2 atmosphere collapses? Is there a layer of noncondensibles that prevents complete collapse?
3. What role does stealth volcanism play in the formation of the atmosphere?
4. How do volcanic plumes interact with Io's atmosphere?
5. How much does surface sputtering contribute to the atmosphere? Are there areas on Io where the atmosphere is collisionally thin, so that ions and electrons from the plasma torus can penetrate down to the surface?
6. What are the origins of NaCl and KCl, and why are they not colocated with SO_2?
7. What is the atmospheric temperature profile (in particular close to the surface), and how does it vary across Io with and without volcanic eruptions?
8. What are the atmospheric wind patterns? Are there large-scale zonal winds, day-to-night winds, and/or rapid winds away from plumes?
9. What are the details on atmospheric loss processes, including atmosphere-magnetosphere connections?
10. What not-yet-detected constituents are present in Io's plume gases?

While a dedicated spacecraft to Io is required to get a full understanding of all physical processes in Io's interior that lead to the observed phenomena, we have made much progress on several of the questions on the interiors/surface posed above by using the more recent ground-based and *HST* observations in combination with spacecraft data and state-of-the-art theoretical models. The extensive data set on volcanic hot spots can be used to improve on Io's heat flow map. A comparison of this map with models on tidal heating already showed that none of the canonical end models for tidal heating match the data beyond the dominance of a degree-2 term in the distribution. More sophisticated models are needed to match the ever-growing data set. Such models will help elucidate the magma ocean hypothesis, where tidal heat is dissipated, and the processes of heat transport to the surface. Observations in the millimeter-to-centimeter range at a high spatial resolution (~0.1", or 300–400 km) are possible now, which in combination with sophisticated models (Section 3.1) would help constrain Io's heat flow and transport mechanism.

As for the atmospheric processes, based on the observations shown in this review, it is clear that volcanoes do have a substantial impact on Io's atmosphere and its dynamics, although overall the atmosphere seems to be driven primarily by sublimation. State-of-the-art atmospheric models combined with millimeter and infrared data of eclipse ingress and egress should help answer several of the atmospheric questions. Without sophisticated modeling, it is already clear from the observations that much of Io's atmosphere collapses within minutes upon eclipse ingress; however, it is not yet clear if the remaining gas is prevented from total collapse by a layer of noncondensible gas or if it is produced by (perhaps stealth) volcanism.

ALMA data in several transitions at a higher spatial resolution would help to unravel the temperature structure close to the surface. Such data are also essential to determine the wind patterns in Io's atmosphere, in particular if there is a prograde horizontal wind; the presence of such a wind was absent in the two ALMA data sets that showed volcanic plumes. A third data set, low in volcanic activity, showed such a potential wind but may be the manifestation of molecules desorbed from the warming rock surface. Wind patterns from volcanic plumes will likely change the overall flow field, but data at a higher spatial resolution are needed to confirm this.

The atmosphere over regions at latitudes poleward of ~40°N/S and over a larger range during eclipse and at night should be thin enough ($<10^{15}$–10^{16} cm^{-2}) for plasma from the Io plasma torus to reach the surface, so that sputtering can contribute to the atmospheric composition. However, because observations of NaCl and KCl seem to be concentrated near volcanic sites, these gases, and their photodissociated products Na, K, and Cl, may preferentially be produced through volcanism. Interestingly, though, these sites usually do not show emissions from SO or SO_2, indicative of differences in the melt composition at different volcanic sites, if NaCl and KCl are indeed sourced through volcanism.

We already alluded to the fact that higher spatial resolution and sensitivity data can be obtained with ALMA now, while longer wavelength data can be obtained with the Very Large Array (VLA). The next-generation VLA will be an order of magnitude more sensitive and have a spatial resolution that is 10 times higher than the VLA and ALMA (at overlapping frequencies) and hence will be a powerful instrument for continuum (sub)surface mapping, detecting new species in the atmosphere, and helping constrain the spatial distribution of known species (and with that the temperature structure and wind field). After the launch of the *James Webb Space Telescope* (*JWST*), it will be easier to carry out spatially resolved observations of Io at visible and infrared wavelengths while in eclipse (no guide stars are needed, removing a limitation on equivalent AO data). The 1.7-μm emission band of SO will be observed during *JWST*'s Early Release Science program (ERS #1373). In the mid-infrared, the difficult-to-observe-from-the-ground SO_2 ν_1 and ν_3 bands at 8.6 and 7.3 μm will also be observed to help disentangle temperature and abundance

effects. The next-generation optical-infrared telescopes will be of order three times larger than the present 8- to 10-m telescopes and hence have a spatial resolution approximately three times higher (assuming AO is utilized) and a sensitivity an order of magnitude larger than the largest telescopes operating now. Interferometric techniques on existing large telescopes, such as Matisse on the VLT, yield much promise for superb high spatial resolution data of very bright eruptions on Io, while carefully planned observations of Io occultations by another moon can extend the timeline of the extremely high-resolution data of Loki Patera (de Kleer et al. 2017) and extend such mappings to other volcanic centers.

DISCLOSURE STATEMENT

The authors are not aware of any affiliations, memberships, funding, or financial holdings that might be perceived as affecting the objectivity of this review.

ACKNOWLEDGMENTS

This research was supported by the National Science Foundation, NSF grant AST-1313485 to the University of California, Berkeley. A portion of this research was carried out at the Jet Propulsion Laboratory, California Institute of Technology, under a contract with the National Aeronautics and Space Administration (80NM0018D0004).

LITERATURE CITED

Ahern AA, Radebaugh J, Christiansen EH, Harris RA, Tass S. 2017. Lineations and structural mapping of Io's paterae and mountains: implications for internal stresses. *Icarus* 297:14–32

Aksnes K, Franklin FA. 2001. Secular acceleration of Io derived from mutual satellite events. *Astron. J.* 122:2734–39

Anderson JD, Jacobson RA, Lau EL, Moore WB, Schubert G. 2000. Io's gravity field and interior structure. *J. Geophys. Res.* 106(E12):32963–69

Bagenal F, Dols V. 2019. The space environment of Io and Europa. *J. Geophys. Res. Space Phys.* 125:e2019JA027485

Bagenal F, Dowling TE, McKinnon WB. 2004. *Jupiter: The Planet, Satellites and Magnetosphere*. Cambridge, UK: Cambridge Univ. Press

Bierson CJ, Nimmo F. 2016. A test for Io's magma ocean: modeling tidal dissipation with a partially molten mantle. *J. Geophys. Res. Planets* 121:2211–24

Binder AP, Cruikshank DP. 1964. Evidence for an atmosphere on Io. *Icarus* 3:299–305

Bland MT, McKinnon WB. 2016. Mountain building on Io driven by deep faulting. *Nat. Geosci.* 9:429–32

Blöcker A, Saur J, Roth L, Strobel DF. 2018. MHD modeling of the plasma interaction with Io's asymmetric atmosphere. *J. Geophys. Res. Space Phys.* 123:9286–311

Brown ME. 2001. Potassium in Europa's atmosphere. *Icarus* 151:190–95

Brozović M, Nolan MC, Magri C, Folkner WM, Jacobson RA, et al. 2020. Arecibo radar astronometry of the Galilean satellites from 1999 to 2016. *Astron. J.* 159:149

Cantrall C, de Kleer K, de Pater I, Williams DA, Davies AG, Nelson D. 2018. Variability and geologic associations of volcanic activity on Io in 2001–2016. *Icarus* 312:267–94

Carlson RW, Kargel JS, Douté S, Soderblom LA, Dalton B. 2007. Io's surface composition. See Lopes & Spencer 2007, pp. 193–229

Carlson RW, Smythe WD, Lopes-Gautier RMC, Davies AG, Kamp LW, et al. 1997. Distribution of sulfur dioxide and other infrared absorbers on the surface of Io. *Geophys. Res. Lett.* 24:2479–82

Carr MH. 1986. Silicate volcanism on Io. *J. Geophys. Res.* 91(B3):3521–32

Cheng AF, Johnson RE. 1989. Effects of magnetospheric interactions on origin and evolution of atmospheres. In *Origin and Evolution of Planetary and Satellites Atmospheres*, ed. SK Atreya, JB Pollack, MS Matthews, pp. 683–722. Tucson: Univ. Ariz. Press

Conrad A, de Kleer K, Leisenring J, La Camera A, Arcidiacomo C, et al. 2015. Spatially resolved M-band emission from Io's Loki Patera–Fizeau imaging at the 22.8 m LBT. *Astron. J.* 149:175

Constable S, Constable C. 2004. Observing geomagnetic induction in magnetic satellite measurements and associated implications for mantle conductivity. *Geochem. Geophys. Geosyst.* 5:Q01006

Cruikshank DP, Nelson RM. 2007. A history of the exploration of Io. See Lopes & Spencer 2007, pp. 5–33

Darwin GH. 1899. The theory of the figure of the Earth carried to the second order of small quantities. *MNRAS* 60:82–124

Davies AG. 1996. Io's volcanism: thermo-physical models of silicate lavas compared with observations of thermal emission. *Icarus* 124:45–61

Davies AG. 2003. Temperature, age and crust thickness distributions of Loki Patera on Io from *Galileo* NIMS data: implications for resurfacing mechanism. *Geophys. Res. Lett.* 30:2133–36

Davies AG. 2007. *Volcanism on Io: A Comparison with Earth*. Cambridge, UK: Cambridge Univ. Press

Davies AG, Davies RL, Veeder GJ, de Kleer K, de Pater I, et al. 2018. Discovery of a powerful, transient, explosive thermal event at Marduk Fluctus, Io, in *Galileo* NIMS data. *Geophys. Res. Lett.* 45:2926–33

Davies AG, Keszthelyi LP, Harris AJL. 2010. The thermal signature of volcanic eruptions on Io and Earth. *J. Volcanol. Geotherm. Res.* 194:75–99

Davies AG, Keszthelyi LP, McEwen AS. 2016. Determination of eruption temperature of Io's lavas using lava tube skylights. *Icarus* 278:266–78

Davies AG, Keszthelyi LP, Williams DA, Phillips CB, McEwen AS, et al. 2001. Thermal signature, eruption style, and eruption evolution at Pele and Pillan on Io. *J. Geophys. Res.* 106(E12):33079–104

Davies AG, Lopes-Gautier R, Smythe WD, Carlson RW. 2000. Silicate cooling model fits to Galileo NIMS data of volcanism on Io. *Icarus* 148:211–25

Davies AG, Veeder GJ, Matson DL, Johnson TV. 2012. Io: charting thermal emission variability with the *Galileo* NIMS Io Thermal Emission Database (NITED): Loki Patera. *Geophys. Res. Lett.* 39:L01201

Davies AG, Veeder GJ, Matson DL, Johnson TV. 2015. Map of Io's volcanic heat flow. *Icarus* 262:67–78

de Kleer K, Butler B, de Pater I, Gurwell MA, Moullet A, et al. 2021. Ganymede's surface properties from millimeter and infrared thermal emission. *Planet. Sci. J.* 2:5

de Kleer K, de Pater I. 2016a. Spatial distribution of Io's volcanic activity from Near-IR adaptive optics observations on 100 nights in 2013–2015. *Icarus* 280:405–14

de Kleer K, de Pater I. 2016b. Time variability of Io's volcanic activity from near-IR adaptive optics observations on 100 nights in 2013–2015. *Icarus* 280:378–404

de Kleer K, de Pater I. 2017. Io's Loki Patera: modeling of three brightening events in 2013–2016. *Icarus* 289:181–98

de Kleer K, de Pater I, Ádámkovics M. 2019a. Emission from volcanic SO gas on Io at high spectral resolution. *Icarus* 317:104–20

de Kleer K, de Pater I, Davies AG, Ádámkovics M. 2014. Near-infrared monitoring of Io & detection of a violent outburst on 29 August 2013. *Icarus* 242:352–64

de Kleer K, de Pater I, Molter E, Banks E, Davies AG, et al. 2019b. Io's volcanic activity from time-domain adaptive optics observations: 2013–2018. *Astron. J.* 158:29

de Kleer K, Nimmo F, Kite E. 2019c. Variability in Io's volcanism on timescales of periodic orbital changes. *Geophys. Res. Lett.* 46:6327–32

de Kleer K, Park R, McEwen AS. 2019d. *Tidal heating: lessons from Io and the Jovian system*. Final Rep. Keck Inst. Space Stud.

de Kleer K, Skrutskie M, Leisenring J, Davies AG, Conrad A, et al. 2017. Complex volcanic resurfacing at Io's Loki Patera. *Nature* 545:199–202

de Pater I, Butler B, Sault RJ, Moullet A, Moeckel C, et al. 2018. Potential for solar system science with the ngVLA. *Science with a Next-Generation VLA*, ed. EJ Murphy, pp. 49–72. San Francisco: ASP

de Pater I, Davies AG, Ádámkovics M, Ciardi DR. 2014. Two new, rare, high-effusion outburst eruptions at Rarog and Heno Paterae on Io. *Icarus* 242:365–78

de Pater I, Davies AG, Marchis F. 2016. Keck observations of eruptions on Io in 2003–2005. *Icarus* 274:284–96
de Pater I, de Kleer K, Ádámkovics M. 2020a. High spatial and spectral resolution observations of the forbidden 1.707 μm Rovibronic SO emissions on Io: evidence for widespread stealth volcanism. *Planet. Sci. J.* 1:29
de Pater I, de Kleer K, Davies AG, Ádámkovics M. 2017. Three decades of Loki Patera observations. *Icarus* 297:265–81
de Pater I, Luszcz-Cook S, Rojo P, Redwing E, de Kleer K, Moullet A. 2020b. ALMA observations of Io going into and coming out of eclipse. *Planet. Sci. J.* 1:60
de Pater I, Marchis F, Macintosh BA, Roe HG, Le Mignant D, et al. 2004. Keck AO observations of Io in and out of eclipse. *Icarus* 169:250–63
de Pater I, Roe HG, Graham JR, Strobel DF, Bernath P. 2002. Detection of the forbidden SO $a^1\Delta \rightarrow X^3\Sigma^-$ Rovibronic transition on Io at 1.7 μm. *Icarus* 156:296–301
Douté S, Schmitt B, Lopes-Gautier R, Carlson R, Soderblom L, et al. 2001. Mapping SO_2 frost on Io by the modeling of NIMS hyperspectral images. *Icarus* 149:107–32
Fanale FP, Banerdt W, Elson L, Johnson TV, Zurek R. 1982. Io's surface: its phase composition and influence on Io's atmosphere and Jupiter's magnetosphere. In *Satellites of Jupiter*, ed. D Morrison, pp. 756–81. Tucson: Univ. Ariz. Press
Feaga LM, McGrath M, Feldman PD. 2009. Io's dayside SO_2 atmosphere. *Icarus* 201:570–84
Fegley B, Zolotov MY. 2000. Chemistry of sodium, potassium, and chlorine in volcanic gases on Io. *Icarus* 148:193–210
Gaskell RW, Synnott SP, McEwen AS, Schaber GG. 1988. Large-scale topography of Io: implications for internal structure and heat transfer. *Geophys. Res. Lett.* 15:581–84
Geissler P, McEwen AS, Keszthelyi L, Lopes-Gautier R, Granahan J, Simonelli P. 1999. Global color variations on Io. *Icarus* 140:265–82
Geissler P, McEwen AS, Phillips CB, Keszthelyi LP, Spencer J. 2004a. Surface changes on Io during the Galileo mission. *Icarus* 169:29–64
Geissler P, McEwen AS, Phillips CB, Simonelli D, Lopes RMC, Douté S. 2001. Galileo imaging of SO_2 frost on Io. *J. Geophys. Res.* 16(E12):33253–66
Geissler P, McEwen AS, Porco C, Strobel DF, Saur J, et al. 2004b. Cassini observations of Io's visible aurorae. *Icarus* 172:127–40
Goldstein SJ, Jacobs KC. 1995. A recalculation of the secular acceleration of Io. *Astron. J.* 110:3054–57
Gratiy SL, Walker AC, Levin DA, Goldstein DB, Verghese PL, et al. 2010. Multi-wavelength simulations of atmospheric radiation from Io with a 3-D spherical-shell backward Monte Carlo radiative transfer model. *Icarus* 207:394–408
Grava C, Schneider NM, Leblanc F, Morgenthaler JP, Mangano V, Barbieri C. 2014. Solar control of sodium escape from Io. *J. Geophys. Res. Planets* 119:404–15
Hamilton CW, Beggan CD, Still S, Beuthe M, Lopes RM, et al. 2013. Spatial distribution of volcanoes on Io: implications for tidal heating and magma ascent. *Earth Planet. Sci. Lett.* 361:272–86
Hay HCFC, Matsuyama I. 2019. Nonlinear tidal dissipation in the subsurface oceans of Enceladus and other icy satellites. *Icarus* 319:68–85
Hood LL, Herbert F, Sonett CP. 1982. The deep lunar electrical conductivity profile: structural and thermal inferences. *J. Geophys. Res.* 87(B7):5311–26
Howell RR. 1997. Thermal emission from lava flows on Io. *Icarus* 127:394–407
Howell RR, Spencer J, Goguen J, Marchis F, Prangé R, et al. 2001. Ground-based observations of volcanism on Io in 1999 and early 2000. *J. Geophys. Res.* 106(E12): 33129–40
Ingersoll AP, Summers ME, Schlipf SG. 1985. Supersonic meteorology of Io: sublimation-driven flow of SO_2. *Icarus* 64:375–90
Jacobson RA. 2013. The gravitational fields of the Galilean satellites—revisited. *Div. Planet. Sci.* 45:418.06
Jessup KL, Spencer JR, Yelle R. 2007. Sulfur volcanism on Io. *Icarus* 192:24–40
Johnson TV, Matson DL, Blaney DL, Veeder GJ, Davies A. 1995. Stealth plumes on Io. *Geophys. Res. Lett.* 22:3293–96
Johnson TV, Veeder GJ, Matson DL, Brown RH, Nelson RM, Morrison D. 1988. Io: evidence for silicate volcanism in 1986. *Science* 242:1280–83

Keane JT, de Kleer K, Rathbun J, Radebaugh J. 2018. *Comprehensive spherical harmonic analysis of the distribution of Io's volcanoes, mountains, heat flow, and other geologic phenomena*. Abstract #P53C-2983, Am. Geophys. Union, Fall Meet.

Kerton CR, Fanale FP, Salvail JR. 1996. The state of SO_2 on Io's surface. *J. Geophys. Res.* 101(E3):7555–63

Keszthelyi L, McEwen AS, Phillips CB, Milazzo M, Geissler P, et al. 2001. Imaging of volcanic activity on Jupiter's moon Io by Galileo during the Galileo Europa Mission and the Galileo Millennium Mission. *J. Geophys. Res.* 106(E12):33025–52

Keszthelyi L, McEwen AS, Taylor GJ. 1999. Revisiting the hypothesis of a mushy global magma ocean in Io. *Icarus* 141(2):415–19

Khan A, Connolly JAD, Pommier A, Noir J. 2014. Geophysical evidence for melt in the deep lunar interior and implications for lunar evolution. *J. Geophys. Res. Planets* 119:2197–221

Khurana KK, Jia X, Kivelson MG, Nimmo F, Schubert G, Russell CT. 2011. Evidence of a global magma ocean in Io's interior. *Science* 332:1186–89

Khurana KK, Kivelson MG, Stevenson DJ, Schubert G, Russell CT, et al. 1998. Induced magnetic fields as evidence for subsurface oceans in Europa and Callisto. *Nature* 395:777–80

Kirchoff MR, McKinnon WB. 2009. Formation of mountains on Io: variable volcanism and thermal stresses. *Icarus* 201:598–614

Kirchoff MR, McKinnon WB, Bland MT. 2020. Effects of faulting on crustal stresses during mountain formation on Io. *Icarus* 335:113326

Kirchoff MR, McKinnon WB, Schenk PM. 2011. Global distribution of volcanic centers and mountains on Io: control by asthenospheric heating and implications for mountain formation. *Earth Planet. Sci. Lett.* 301:22–30

Kivelson MG, Khurana KK, Russell CT, Volwerk M, Walker RJ, Zimmer C. 2000. Galileo magnetometer measurements: a stronger case for a subsurface ocean at Europa. *Science* 289:1340–43

Kivelson MG, Khurana KK, Volwerk M. 2002. The permanent and inductive magnetic moments of Ganymede. *Icarus* 157:507–22

Kliore A, Cain DL, Fjeldbo G, Seidel BL, Rasool SI. 1974. Preliminary results on the atmospheres of Io and Jupiter from the *Pioneer 10* S-Band occultation experiment. *Science* 183:323–24

Lainey V, Arlot J, Karatekin Ö, van Hoolst T. 2009. Strong tidal dissipation in Io and Jupiter from astrometric observations. *Nature* 459:957–59

Laver C, de Pater I. 2009. The global distribution of sulfur dioxide ice on Io, observed with OSIRIS on the W.M. Keck telescope. *Icarus* 201:172–81

Lellouch E. 1996. Urey Prize Lecture. Io's atmosphere: not yet understood. *Icarus* 124:1–21

Lellouch E, Ali-Dib M, Jessup K-L, Smette A, Käufl H-U, Marchis F. 2015. Detection and characterization of Io's atmosphere from high-resolution 4-μm spectroscopy. *Icarus* 253:99–114

Lellouch E, Belton MJS, de Pater I, Gulkis S, Encrenaz T. 1990. Io's atmosphere from microwave detection of SO_2. *Nature* 346:639–41

Lellouch E, Belton MJS, de Pater I, Paubert G, Gulkis S, Encrenaz T. 1992. The structure, stability, and global distribution of Io's atmosphere. *Icarus* 98:271–95

Lellouch E, McGrath MA, Jessup KL. 2007. Io's atmosphere. See Lopes & Spencer 2007, pp. 231–64

Lellouch E, Paubert G, Moses JI, Schneider NM, Strobel DF. 2003. Volcanically emitted sodium chloride as a source for Io's neutral clouds and plasma torus. *Nature* 421:45–47

Linde AT, Sacks IS. 1998. Triggering of volcanic eruptions. *Nature* 395:888–90

Lopes RMC, Spencer JR, eds. 2007. *Io After* Galileo*: A New View of Jupiter's Volcanic Moon*. Berlin: Springer

Macintosh B, Gavel D, Gibbard SG, Max CE, de Pater I, et al. 2003. Speckle imaging of volcanic hot spots on Io with the Keck telescope. *Icarus* 165:137–43

Marchis F, de Pater I, Davies AG, Roe HG, Fusco T, et al. 2002. High-resolution Keck adaptive optics imaging of violent volcanic activity on Io. *Icarus* 160:124–31

Matson DL, Davies AG, Veeder GJ, Rathbun JA, Johnson TV, Castillo JC. 2006. Io: Loki Patera as a magma sea. *J. Geophys. Res.* 111(E9):E09002

Matson DL, Ransford GA, Johnson TV. 1981. Heat flow from Io (JI). *J. Geophys. Res.* 86(B3):1664–72

Matsuyama I, Beuthe M, Hay HCFC, Nimmo F, Kamata S. 2018. Ocean tidal heating in icy satellites with solid shells. *Icarus* 312:208–30

McDoniel WJ, Goldstein DB, Varghese PL, Trafton LM. 2017. The interaction of Io's plumes and sublimation atmosphere. *Icarus* 294:81–97

McEwen AS, Keszthelyi L, Spencer JR, Schubert G, Matson DL, et al. 1998. High-temperature silicate volcanism on Jupiter's moon Io. *Science* 281:87–90

McEwen AS, Soderblom LA, Johnson TV, Matson DL. 1988. The global distribution, abundance, and stability of SO_2 on Io. *Icarus* 75:450–78

McGrath MA, Belton MJS, Spencer JR, Sartoretti P. 2000. Spatially resolved spectroscopy of Io's Pele plume and SO_2 atmosphere. *Icarus* 146:476–93

McKinnon WB, Schenk PM, Dombard AJ. 2001. Chaos on Io: a model for formation of mountain blocks by crustal heating, melting, and tilting. *Geology* 29:103–6

Mendillo M, Baumgardner J, Flynn B, Hughes WJ. 1990. The extended sodium nebula of Jupiter. *Nature* 348:312–14

Moore C, Goldstein DB, Varghese P, Trafton L, Stewart B. 2009. 1-D DSMC simulation of Io's atmospheric collapse in eclipse. *Icarus* 201:585–97

Moore WB, Schubert G, Anderson JD, Spencer JR. 2007. The interior of Io. See Lopes & Spencer 2007, pp. 90–108

Morabito LA, Synnott SP, Kupferman PN, Collins SA. 1979. Discovery of currently active extraterrestrial volcanism. *Science* 204:972

Morrison D, Cruikshank DP. 1973. Thermal properties of the Galilean satellites. *Icarus* 18:224–36

Moses JI, Nash DB. 1991. Phase transformations and the spectral reflectance of solid sulfur—Can metastable sulfur allotropes exist on Io? *Icarus* 89:277–304

Moses JI, Zolotov MY, Fegley B. 2002a. Alkali and chlorine photochemistry in a volcanically driven atmosphere on Io. *Icarus* 156:107–35

Moses JI, Zolotov MY, Fegley B. 2002b. Photochemistry of a volcanically driven atmosphere on Io: sulfur and oxygen species from a Pele-type eruption. *Icarus* 156:76–106

Moullet A, Gurwell MA, Lellouch E, Moreno R. 2010. Simultaneous mapping of SO_2, SO, NaCl in Io's atmosphere with the Submillimeter Array. *Icarus* 208:353–65

Moullet A, Lellouch E, Gurwell M, Moreno R, Black J, Butler B. 2015. *Distribution of alkali gases in Io's atmosphere*. Abstract #311.31, AAS Div. Planet. Sci. Meet.

Moullet A, Lellouch E, Moreno R, Gurwell MA, Black JH, Butler B. 2013. Exploring Io's atmospheric composition with APEX: first measurement of $^{34}SO_2$ and tentative detection of KCl. *Astrophys. J.* 776:32

Moullet A, Lellouch E, Moreno R, Gurwell MA, Moore C. 2008. First disk-resolved millimeter observations of Io's surface and SO_2 atmosphere. *Astrophys. Astron.* 482:279–92

Mura A, Adriani A, Tosi F, Lopes RMC, Sindoni G, et al. Infrared observations of Io from Juno. *Icarus* 341:113607

Murray CD, Dermott SF. 1999. *Solar System Dynamics*. Cambridge, UK: Cambridge Univ. Press

Nimmo F, Pappalardo RT. 2016. Ocean worlds in the outer solar system. *J. Geophys. Res. Planets* 121:1378–99

Oberst J, Schuster P. 2004. Vertical control point network and global shape of Io. *J. Geophys. Res.* 109(E4):E04003

O'Reilly TC, Davies GF. 1981. Magma transport of heat on Io: a mechanism allowing a thick lithosphere. *Geophys. Res. Lett.* 8:313–16

Peale SJ, Cassen P, Reymolds RT. 1979. Melting of Io by tidal dissipation. *Science* 203:892–94

Pearl JC, Hanel R, Kunde V, Maguire W, Fox K, et al. 1979. Identification of gaseous SO_2 and new upper limits for other gases on Io. *Nature* 288:757–58

Pommier A, Leinenweber K, Tasaka M. 2015. Experimental constraints on the electrical anisotropy of the lithosphere–asthenosphere system. *Nature* 522(7555):202–6

Rathbun JA, Spencer JR. 2006. Loki, Io: new ground-based observations and a model describing the change from periodic overturn. *Geophys. Res. Lett.* 33:L17201

Rathbun JA, Spencer JR, Davies AG, Howell RR, Wilson L. 2002. Loki, Io: a periodic volcano. *Geophys. Res. Lett.* 29:84-1–84-4

Rathbun JA, Spencer JR, Tamppari LK, Martin TZ, Barnard L, Travis LD. 2004. Mapping of Io's thermal radiation by the Galileo photopolarimeter-radiometer (PPR) instrument. *Icarus* 169:127–39

Redwing E, de Pater I, Luszcz-Cook S, Moullet A, Rojo P, de Kleer K. 2020. *Observations and analysis of NaCl and KCl in Io's atmosphere*. Abstract P031-06, Am. Geophys. Union, Fall Meet.
Renaud JP, Henning WG. 2018. Increased tidal dissipation using advanced rheological models: implications for Io and tidally active exoplanets. *Astrophys. J.* 857:98
Ross MN, Schubert G, Spohn T, Gaskell RW. 1990. Internal structure of Io and the global distribution of its topography. *Icarus* 85:309–25
Roth L, Boissier B, Moullet A, Sánchez-Monge Á, de Kleer K, et al. 2020. An attempt to detect transient changes in Io's SO_2 and NaCl atmosphere. *Icarus* 350:113925
Roth L, Saur J, Retherford KD, Blöcker A, Strobel DF, Feldman PD. 2017. Constraints on Io's interior from auroral spot oscillations. *J. Geophys. Res. Space Phys.* 122:1903–27
Roth L, Saur J, Retherford KD, Feldman PD, Strobel DF. 2014. A phenomenological model of Io's UV aurora based on HST/STIS observations. *Icarus* 228:386–406
Sagan C. 1979. Sulphur flows on Io. *Nature* 280:750–53
Saur J, Duling S, Roth L, Jia X, Strobel DF, et al. 2015. The search for a subsurface ocean in Ganymede with Hubble Space Telescope observations of its auroral ovals. *J. Geophys. Res. Space Phys.* 120:1715–37
Schaefer L, Fegley B. 2004. A thermodynamic model of high temperature lava vaporization on Io. *Icarus* 169:216–41
Schaefer L, Fegley B. 2005. Alkali and halogen chemistry in volcanic gases on Io. *Icarus* 173:454–68
Schenk P, Hargitai H, Wilson R, McEwen A, Thomas P. 2001. The mountains of Io: global and geological perspectives from Voyager and Galileo. *J. Geophys. Res.* 106(E12):33201–22
Schmitt B, de Bergh C, Lellouch E, Maillard J-P, Barbe A, Douté S. 1994. Identification of three absorption bands in the 2-μm spectrum of Io. *Icarus* 111:79–105
Schubert G, Anderson JD, Spohn T, McKinnon WB. 2004. Interior composition, structure and dynamics of the Galilean satellites. See Bagenal et al. 2004, pp. 281–306
Šebek O, Trávníček PM, Walker RJ, Hellinger P. 2019. Dynamic plasma interaction at Io: multispecies hybrid simulations. *J. Geophys. Res. Space Phys.* 124:313–41
Secosky JJ, Potter M. 1994. A Hubble Space Telescope study of posteclipse brightening and albedo changes on Io. *Icarus* 111:73–78
Segatz M, Spohn T, Ross MN, Schubert G. 1988. Tidal dissipation, surface heat flow, and figure of viscoelastic models of Io. *Icarus* 75:187–206
Sinton WM, Kaminsky C. 1988. Infrared observations of eclipses of Io, its thermophysical parameters, and the thermal radiation of the Loki volcano and environs. *Icarus* 75:207–32
Soderlund KM, Schmidt BE, Wicht J, Blankenship DD. 2014. Ocean-driven heating of Europa's icy shell at low latitudes. *Nat. Geosci.* 7:16–19
Spencer DC, Katz RF, Hewitt IJ. 2020. Magmatic intrusions control Io's crustal thickness. *J. Geophys. Res. Planets* 125:e2020JE006443
Spencer JR, Lellouch E, Richter MJ, López-Valverde MA, Jessup KL, et al. 2005. Mid-infrared detection of large longitudinal asymmetries in Io's SO_2 atmosphere. *Icarus* 176:283–304
Spencer JR, Rathbun JA, Travis LD, Tamppari LK, Barnard L, et al. 2000. Io's thermal emission from the Galileo photopolarimeter-radiometer. *Science* 288:1198–201
Steinke T, Hu H, Höning D, van der Wal W, Vermeersen BLA. 2020. Tidally induced lateral variations of Io's interior. *Icarus* 335:113299
Steinke T, van der Wal W, Vermeersen BLA. 2019. *Modelling the feedback of Io's tidally induced heterogeneous interior on tidal dissipation*. Abstract P51A-07, Am. Geophys. Union, Fall Meet.
Strobel DF, Zhu X, Summers ME. 1994. On the vertical structure of Io's atmosphere. *Icarus* 111:18–30
Summers ME, Strobel DF. 1996. Photochemistry and vertical transport in Io's atmosphere and ionosphere. *Icarus* 120:290–316
Tackley PJ, Schubert G, Glatzmaier GA, Schenk P, Ratcliff J, et al. 2001. Three-dimensional simulations of mantle convection in Io. *Icarus* 149:79–93
Tobie G, Mocquet A, Sotin C. 2005. Tidal dissipation within large icy satellites: applications to Europa and Titan. *Icarus* 177(2):534–49
Tosi F, Mura A, Lopes RMC, Filacchione G, Ciarniello M. 2020. Mapping Io's surface composition with Juno/JIRAM. *J. Geophys. Res. Planets* 125:e2020JE006522

Tsang CCC, Spencer JR, Lellouch E, Lopez-Valverde MA, Richter MJ. 2016. The collapse of Io's primary atmosphere in Jupiter eclipse. *J. Geophys. Res. Planets* 121:1400–10

Tsang CCC, Spencer JR, Lellouch E, Lopez-Valverde MA, Richter MJ, Greathouse TK. 2012. Io's atmosphere: constraints on sublimation support from density variations on seasonal timescales using NASA IRTF/TEXES observations from 2001 to 2010. *Icarus* 217:277–96

Turtle EP, Jaegar WL, Schenk PM. 2007. Ionian mountains and tectonics: insights into what lies beneath Io's lofty peaks. See Lopes & Spencer 2007, pp. 109–28

Tyler RH, Henning WG, Hamilton CW. 2015. Tidal heating in a magma ocean within Jupiter's moon Io. *Astrophys. J. Suppl.* 218:22

Veeder GJ, Davies AG, Matson DL, Johnson TV, Williams DA, Radebaugh J. 2012. Io: volcanic thermal sources and global heat flow. *Icarus* 219:701–22

Veeder GJ, Davies AG, Matson DL, Johnson TV, Williams DA, Radebaugh J. 2015. Io: heat flow from small volcanic features. *Icarus* 245:379–410

Veeder GJ, Matson DL, Johnson TV, Blaney DL, Goguen JD. 1994. Io's heat flow from infrared photometry:, 1983–1993. *J. Geophys. Res.* 99(E8):17095–162

Wagman DD. 1979. *Sublimation Pressure and Enthalpy of SO_2*. Data sheet, Chem. Thermodyn. Data Cent., Washington, DC, Nat. Bur. Stand.

Walker AC, Gratiy SL, Goldstein DB, Moore CH, Varghese PL, et al. 2010. A comprehensive numerical simulation of Io's sublimation-driven atmosphere. *Icarus* 207:409–32

Walker AC, Moore CH, Goldstein DB, Varghese PL, Trafton LM. 2012. A parametric study of Io's thermophysical surface properties and subsequent numerical atmospheric simulations based on the best fit parameters. *Icarus* 220:225–53

White OL, Schenk PM, Nimmo F, Hoogenboom T. 2014. A new stereo topographic map of Io: implications for geology from global to local scales. *J. Geophys. Res. Planets* 119:1276–301

Wieczorek MA. 2015. Gravity and topography of the terrestrial planets. In *Treatise on Geophysics*, ed. G Schubert, pp. 153–93. Amsterdam: Elsevier. 2nd ed.

Williams DA, Davies AG, Keszthelyi LP, Greeley R. 2001. The summer 1997 eruption at Pillan Patera on Io: implications for ultrabasic lava flow emplacement. *J. Geophys. Res.* 106(E12):33105–20

Williams DA, Keszthelyi LP, Crown DA, Yff JA, Jaeger WL, et al. 2011. *Geologic Map of Io*. U.S. Geological Survey Scientific Investigations Map 3168, scale 1:15,000,000, **https://pubs.usgs.gov/sim/3168/**

Wu RCY, Yang BW, Chen FZ, Judge J, Caldwell J, Trafton LM. 2000. Measurements of high-, room-, and low-temperature photoabsorption cross sections of SO_2 in the 2080- to 2950-A region, with applications to Io. *Icarus* 145:289–96

Yoshikawa I, Yoshioka K, Murakami F, Yamazaki A, Tsuchiya F, et al. 2014. Extreme ultraviolet radiation measurement for planetary atmospheres, magnetospheres from Earth-orbiting spacecraft (EXCEED). *Space Sci. Rev.* 184:237–58

Yoshioka K, Tsuchiya F, Kagitani M, Kimura T, Murakami G. 2018. The influence of Io's 2015 volcanic activity on Jupiter's magnetospheric dynamics. *Geophys. Res. Lett.* 45:10195–99

Zhang J, Goldstein DB, Varghese PL, Gimelshein NE, Gimelshein SF, Levin DA. 2003. Simulation of gas dynamics and radiation in volcanic plumes of Io. *Icarus* 163:182–87

Zhang J, Goldstein DB, Varghese PL, Trafton L, Moore C, Miki K. 2004. Numerical modeling of Ionian volcanic plumes with entrained particulates. *Icarus* 172:479–502

Zimmer C, Khurana KK, Kivelson MG. 2000. Subsurface oceans on Europa and Callisto: constraints from Galileo magnetometer observations. *Icarus* 147.2:329–47

Zolotov MY, Fegley B Jr. 1998. Volcanic production of sulfur monoxide (SO) on Io. *Icarus* 132:431–34

Zolotov MY, Fegley B Jr. 2000. Eruption conditions of Pele volcano on Io inferred from chemistry of its volcanic plume. *Geophys. Res. Lett.* 27:2789–92